2015-11-01

# Design and Manufacture of Mesoscale Robot-Actuated Surgical Instruments

Clayton L. Grames
*Brigham Young University - Provo*

# Design and Manufacture of Mesoscale Robot-Actuated Surgical Instruments

Clayton L. Grames

A thesis submitted to the faculty of
Brigham Young University
in partial fulfillment of the requirements for the degree of

Master of Science

Spencer P. Magleby, Chair
Brian D. Jensen
Larry L. Howell

Department of Mechanical Engineering

Brigham Young University

November 2015

ABSTRACT

Design and Manufacture of Mesoscale Robot-Actuated Surgical Instruments

Clayton L. Grames
Department of Mechanical Engineering, BYU
Master of Science

Minimally Invasive Surgery (MIS) is a growing field including both laparoscopic and robotic operations. Surgeons and engineers are making continual efforts to reduce the negative effects of procedures on patients. Reducing the size of the surgical instruments is one effective method pursued in this effort. When the instruments approach 3 mm in diameter, they reach a threshold where the entry incisions can be small enough that no scar is left on the patient. Laparoscopic instruments on this scale exist but typically lack wrist articulation and only have 1 degree of freedom (DoF). Alternatively, robotic surgical instruments can achieve high levels of dexterity but at a greater diameter. Smaller diameter robotic instruments employ snake wrists but this results in large swept volumes. There is a need for smaller robotic instruments with 3 DoF that preserve a small operational volume.

Several unique challenges result when trying to develop small-scale instruments. Friction forces due to the relative motion of actuation cables and other parts in the mechanisms become more significant, as do the challenges of producing and assembling parts with extremely small features. These challenges have been limiting factors for the size of instruments. Traditional mechanisms use pin joints and pulleys which result in higher part counts and higher internal friction. To overcome these challenges, two alternative designs that reduce part count and minimize friction are presented as potential mechanisms that could be used as surgical instruments on the mesoscale (1-5 mm). Both designs implement rolling contact and gearing in place of pin joints and pulleys to realize their motion. Additionally, alternative manufacturing methods that are ideally suited to mesoscale production are presented. Micro metal laser sintering and composite carbon nanotude structures are shown to have the resolution required to create the detailed features necessary for these new designs. The result are two mechanisms suited to be produced as mesoscale, robotically actuated, surgical instruments. One of the two designs has been physically prototyped and has demonstrated clinical capabilities at 4 and 5 mm diameter instrument sizes.

Keywords: surgical instruments, robotics, mesoscale, healthcare, medical devices

# ACKNOWLEDGMENTS

This research has been funded by a research grant provided by Intuitive Surgical, Inc. I have been incredibly fortunate to have impeccable technical guidance and support from an involved graduate committee. Drs. Spencer Magleby, Larry Howell, and Brian Jensen have not only been faculty members and educators for much of my engineering education, but active supporters and advisers through every step of my graduate work.

I have also benefited greatly from industry mentors. This work would not have been possible without the input and support of Ryan Steger and Andrew Waterbury who have been pivotal in helping me to bridge the gap from my academic research to the physical world.

I have never been alone in my work as a student researcher. The help, encouragement, and patience from my peers has had a large impact on my ability to transform ideas into reality. I would like to recognize the mentorship of Landen Bowen and Jordan Tanner who encouraged me to be involved and realize my own potential while I was still an undergraduate student. Also, Jason Dearden who has been a great colleague during my last year as a graduate student.

Finally I would like to express gratitude for all those who have provided non-technical support over the years. My family and friends have always been there to cheer me on as I have struggled through finding my place within my own chosen field, particularly my loving parents, Con and Cindy Grames.

TABLE OF CONTENTS

LIST OF TABLES

LIST OF FIGURES

# CHAPTER 1. INTRODUCTION

Minimally Invasive Surgery (MIS) is a growing field including both laparoscopic and robotic operations. Surgeons and engineers are making continual efforts to reduce the negative effects of procedures on patients. Reducing the size of the surgical instruments is one effective method pursued in this effort. When instruments approach 3 mm in diameter, they reach a threshold where the entry incisions can be small enough that no scar is left on the patient [1, 2]. Laparoscopic instruments on this scale exist but typically lack wrist articulation and only have one degree of freedom (DoF) [3, 4]. Alternatively, robotic surgical instruments can achieve high levels of dexterity but at a greater diameter [5]. Smaller diameter robotic instruments employ snake wrists but this results in large swept volumes [6]. There is a need for smaller, mesoscale (1-5 mm in diameter) robotic instruments with 3 DoF that preserve a small operational volume.

## 1.1 Background

For this research existing instruments are categorized in the four quadrants shown in Fig. 1.1. The first three quadrants are well represented by a variety of designs: large instruments (6-10 mm) with 1-2 DoF in quadrant I [7]; small instruments (3 mm or less) with 1-2 DoF in quadrant II [8–13]; and large instruments with 3+ DoF in quadrant III [14–21]. Quadrant IV, defined by mesoscale instruments with articulating wrists, is largely unpopulated.

Many challenges are present in quadrant IV that are not as pertinent in the other three. For example, manufacturing techniques used in the 5-10 mm range are less reliable when dealing with mesoscale parts. The differences in manufacturing techniques between quadrants I and II are a direct result of this reliability challenge [11, 22–24]. In addition to manufacturing, assembly of individual parts at this size is challenging.

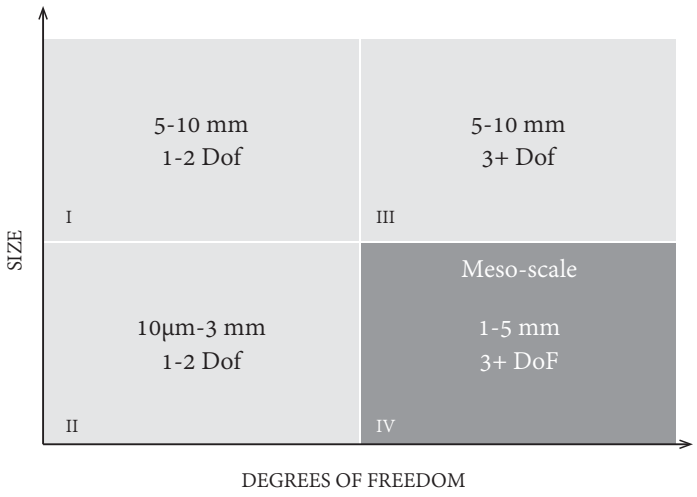


Figure 1.1: Categorization of existing surgical instruments where quadrant IV is mostly unpopulated.

## 1.2 Challenges

There are many challenges with producing surgical instruments. There are even more challenges associated with producing mesoscale robotic surgical instruments. Perhaps foremost among these challenges are the increasing impact of friction at smaller sizes, and the limited resolution in manufacturing methods.

In cable-actuated mechanisms, as the diameter of the instrument is reduced, the available moment arm that can be utilized in actuation of the grips or jaws is also reduced. As a result, higher forces must be implemented to achieve a proportional output force through the mechanism. Traditional mechanisms using pin joints would consequently require larger diameter pins to withstand the increased loading without failure. Increased pin and hole size subsequently lead to increased friction at the interfaces. At smaller scales friction forces become relatively large in comparison to applied forces which in turn increases the required magnitude of the input forces. Thus begins a spiralling effect where input and friction forces are both increasing such that the mechanisms can no longer function.

Mesoscale mechanisms necessitate small features to be manufactured with a level of precision and tolerance control that allows them to be assembled and still function. Traditional mech-

anism architectures using pin joints and pulleys result in a high part count. This results in small features and complex assemblies. Standard methods of manufacturing cannot cost effectively produce these parts with the tolerances required for robust mechanisms.

## 1.3 Approach

In order to overcome these challenges, two designs were developed. They purposefully implement architectures and manufacturing methods that avoid these challenges and result in mesoscale instruments with high dexterity and a large range of motion.

Two novel instrument designs that implement rolling contact and gearing are presented. The first, the Split CORE, is a one DoF wrist combined with a single gripping DoF. The second, the crossed cylinders wrist, is a very compact two DoF wrist. The rolling contact yields high compressive load bearing capacity while the gearing prevents slip from occurring during actuation.

The process used to develop these mechanisms was targeted to overcome the challenges cited previously. The product design requirements were aimed to reduce part count, mitigate friction, and relax assembly sensitivity to geometric variations caused by manufacturing imperfections. Many concept generation methods such as brainstorming and recombination tables were used to create a broad pool of potential designs. The pool was organized into categories to identify potentially overlooked or underdeveloped families of concepts and was followed by additional concept generation to increase the depth of the selection pool. High potential candidates were prototyped in a variety of methods at large scales (5-15X) then evaluated based on the previously defined design requirements. The concepts ranked the highest based on these requirements were then selected for preliminary analysis and testing.

Kinematic analysis not only predicts the motion of any point along the actuated portions of the mechanisms but allows the relationships between the input and output forces to be described mathematically. This allows the designer to know what input forces are required to yield a desired output force at the tip of the instrument jaws.

Analysis on the most critical stress states of each mechanism was completed to show that they can function under expected clinical loading conditions without failure. Additionally, for one of the devices, various disengagement scenarios were analyzed either analytically or experimen-

tally to determine the loads required to failure. Positive results from the kinematic and failure mode analyses acted as a gateway into higher fidelity prototyping.

Physical prototypes were made using both a composite Carbon Nanotube (CNT) structure and a micro Metal Laser Sintering (MLS) method. These methods are both well suited for creating small parts with highly detailed features. These processes, in combination with highly simplified mechanism architectures, allowed for the parts to be prototyped and the instruments to be assembled successfully.

Using these novel manufacturing methods the first mechanism was prototyped in 3, 4, and 5 mm diameter variants. The two larger prototypes were functional prototypes that could be robotically driven and tested. Both sets of prototypes proved to have the strength and force transfer necessary to perform relevant clinical tasks such as manipulating tissue and driving needles and suture.

# CHAPTER 2. THE SPLIT CORE

The Split CORE[1] is a novel instrument design that has been prototyped and tested to demonstrate its clinical relevance.

## 2.1 Design Considerations

The Split CORE is a derivative of the traditional CORE (Compliant Rolling-Element) joint that involves joining two half cylinders with flexures as shown in Fig. 2.1 [25]. The Split CORE replaces the half cylinders with truncated joints to reduce the size of the joint as shown in Figure 2.2. Consequently, this also limits the range of motion to 90 degrees, which is considered acceptable for many surgical applications. In place of flexures the Split CORE uses the input actuation force to maintain compressive contact between the different elements. Additionally, the top half of the joint is split in two to create two distinctly controllable surfaces where individual jaws are mounted. Finally, gearing is added to prevent slip while the joint rolls (Fig. 2.1). This creates a two DoF gripping mechanism—one rotational degree of freedom, and another degree of freedom associated with the opening and closing of the jaws.

The curved surfaces of the upper and lower rolling segments consist of two rows of gear profiles which prevent slip between the two segments and allow precise control of the gripper locations. The curved surfaces also include non-geared areas which support the compressive loads associated with gripper motion and holding the assembly together. Existing surgical instruments have used gearing without the added benefit of rolling contact [26]. The Split CORE design shown on the left of Fig. 2.3 has three distinct non-geared regions. These regions are included in the design so that all compressive loads are transferred away from the gear profiles which would otherwise experience higher stresses because of smaller cross-sections and stress concentrations.

[1]This chapter is largely drawn from the 2015 International Design Engineering Technical Conference article DETC2015-46516 titled *A Mesoscale, Rolling-Contact Gripping Mechanism for Robotic Surgery* with co-authors Jordan D. Tanner, Brian D. Jensen, Spencer P. Magleby, Larry L. Howell, and John Ryan Steger

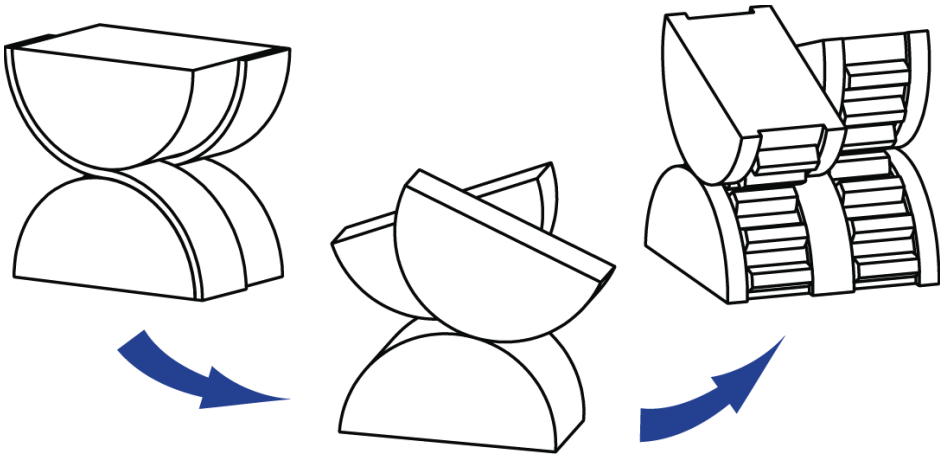

Figure 2.1: Concept development of the split CORE mechanism. LEFT: Traditional CORE joint with flexures MID: CORE joint with split top half and no flexures RIGHT: Gearing added to prevent slip

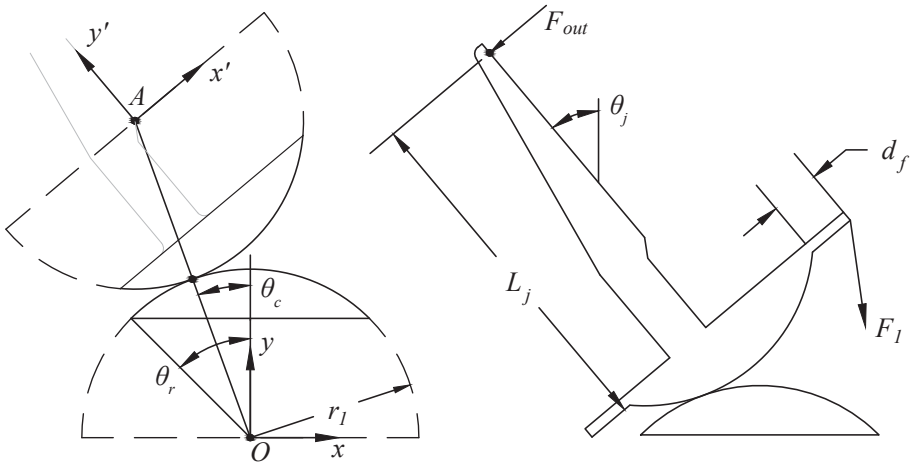


Figure 2.2: Parameters defining the geometry of the Split CORE mechanism

### 2.1.1 Parameters and Geometry

The motion of the Split CORE is most easily modeled when compared to the motion of the traditional CORE joint. The traditional CORE joint is modeled as two half cylinders—a fixed lower segment and a free upper segment which rolls along the curved surface of the lower segment. This is shown in Fig. 2.2 by the dashed lines. The proposed design (Split CORE model) is based on the same principle but uses a smaller portion of the circular arc to reduce the size of the joint,

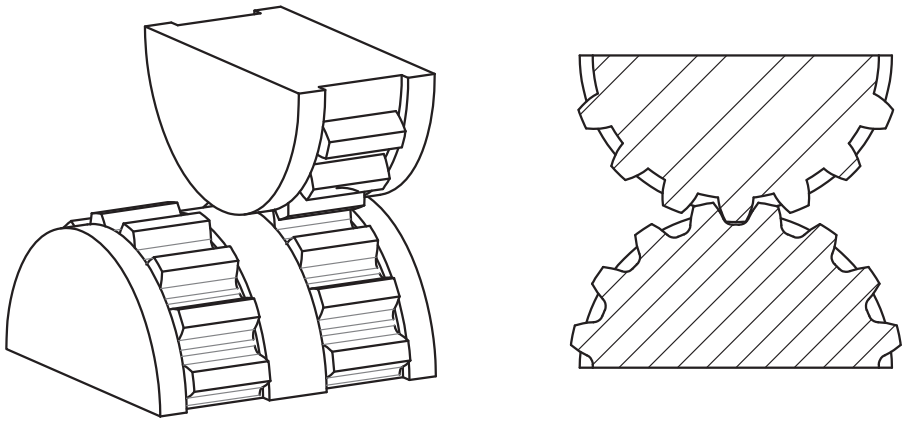

Figure 2.3: LEFT: Three rolling contact surfaces with gearing in between RIGHT: Cross section of meshing gears with rolling contact surfaces at the pitch diameter

and is shown in Fig. 2.2 by the solid lines. The arcs of both the traditional CORE model and the Split CORE model have the same radius of curvature, $r_1$, and are concentric. The centers of the lower and upper segments are labeled as $O$ and $A$, respectively. Although neither of the centers physically exist on the Split CORE model they are used as reference points because they simplify the derivations of equations of motion and force output.

The angle $\theta_r$ is used to describe the size of the arc used in the design. For example, if $\theta_r$ is equal to $90^\circ$ the result would be equivalent to the traditional CORE joint. If $\theta_r$ is equal to $45^\circ$ the resulting mechanism would look similar to the one shown by solid lines in Fig. 2.2.

The parameters of interest are the output force at the jaws, $F_{out}$, the angle of the jaws, $\theta_j$, and the required input forces, $F_1$ and $F_2$. The principle of virtual work is used to determine these input forces for any given values of $F_{out}$ and $\theta_j$ [27]. The angle used to describe the point of contact between the upper and lower segments ($\theta_c$) is also used but can be described as a function of the jaw angle by the following relation:

$$\theta_c = \frac{\theta_j}{2} \tag{2.1}$$

All angles shown in Fig. 2.2 are defined as positive counter-clockwise from the y-axis, and the origin of the coordinate system is at point $O$ as shown. Another coordinate system, $x$'-$y$', is also shown. This system will be used along with a rotation matrix to define the location and direction

of the input forces in terms of the *x*-*y* coordinate system. The origin of the *x*'-*y*' coordinate system is point *A*.

### 2.1.2 Input Forces and Mechanical Advantage

Two input forces exist in this design, $F_1$ and $F_2$, as shown in Fig. 2.2. If the actuating cables attached at the points of $F_1$ and $F_2$ are connected to a common spool, then it is assumed that as a force is applied to one cable the force in the opposite cable goes to zero. In addition to this assumption Fig. 2.2 shows that for any nonzero value of $F_{out}$, $F_1$ will also be nonzero, and consequently $F_2$ will be zero. This is because $F_1$ is the only force that can balance the system. If considering the other jaw in the assembly (not shown in Fig. 2.2), for any nonzero value of $F_{out}$, $F_2$ would be nonzero and $F_1$ would be zero. The derivations that follow apply to the case shown in Fig. 2.2 where $F_2$ is zero. However, the same approach can be used to consider the case for the opposite jaw.

The method of virtual work can be used to determine the magnitude of $F_1$ for given values of $F_{out}$ and $\theta_j$. The jaw angle, $\theta_j$, is chosen as the generalized coordinate because it is used to describe the position of the jaw, and because the expression for $F_1$ will be derived as a function of $\theta_j$. Each of the applied forces can be written in vector form in terms of the generalized coordinate, and the directions of the forces are shown in Eqs. 2.2 and 2.3 for $F_{out}$ and $F_1$, respectively.

$$\mathbf{F_{out}} = F_{out}\left(-\cos\theta_j\hat{\mathbf{i}} - \sin\theta_j\hat{\mathbf{j}}\right) \tag{2.2}$$

$$\mathbf{F_1} = F_1\left(\sin\frac{\theta_j}{2}\hat{\mathbf{i}} - \cos\frac{\theta_j}{2}\hat{\mathbf{j}}\right) \tag{2.3}$$

Position vectors are written from the origin, *O*, to each of the applied forces. The vector describing the location of $Z_{out}$ is straightforward to describe in terms of $\theta_j$ as

$$\mathbf{Z_{out}} = \left[-2r_1\sin\frac{\theta_j}{2} - \left(L_j - r_1\cos\theta_r\right)\sin\theta_j\right]\hat{\mathbf{i}} + \left[2r_1\cos\frac{\theta_j}{2} + \left(L_j - r_1\cos\theta_r\right)\cos\theta_j\right]\hat{\mathbf{j}} \tag{2.4}$$

The other vector is more complicated because it lies at a point on the arc determined by $\theta_r$, and that point is a fraction of $\theta_j$. The position vector locating $\mathbf{Z_1}$ can be found by summing the vector from point $O$ to point $A$ and the vector from point $A$ to the location of force application. This results in the vector describing the position of $Z_1$ as

$$\mathbf{Z_1} = \left[-2r_1 \sin\frac{\theta_j}{2} + r_1 \sin\left(\theta_j + \theta_r\right)\right]\hat{\mathbf{i}} + \left[2r_1 \cos\frac{\theta_j}{2} - r_1 \cos\left(\theta_j + \theta_r\right)\right]\hat{\mathbf{j}} \tag{2.5}$$

The virtual displacement associated with eqs. 2.4-2.5 is their partial derivatives with respect to the generalized coordinate.

The virtual work associated with each force is determined by calculating the dot product of each force vector (Eqs. 2.2 and 2.3) and its respective virtual displacement vector. The sum of these dot products is the total virtual work in the system. For a system in equilibrium, the total virtual work is equal to zero. This makes it possible to rearrange the equation to determine $F_1$ for various values of $F_{out}$ and $\theta_j$, or

$$F_1 = \frac{F_{out}\left(\cos\frac{\theta_j}{2} - \cos\theta_r + \frac{L_j}{r_1}\right)}{\sin\left(\theta_r + \frac{\theta_j}{2}\right)} \tag{2.6}$$

**Including a Preload Force**

In most cases a preload force is applied with the actuation forces (Fig. 2.2). If an equal preload force is applied to both sides of the mechanism (i.e. equal preload in both actuation cables) then the changes to the previous derivations are relatively simple. The input force term, $F_1$, is replaced by $(F_1 + F_p)$ where $F_p$ is the preload force. The virtual work derivation would also include the effects of $F_p$ at the location of $F_2$. Doing this results in a slightly different expression for $F_1$ given by

$$F_1 = \frac{F_{out}\left(\cos\frac{\theta_j}{2} - \cos\theta_r + \frac{L_j}{r_1}\right) - 2F_p r_1 \cos\theta_r \sin\frac{\theta_j}{2}}{\sin\left(\theta_r + \frac{\theta_j}{2}\right)} \tag{2.7}$$

The inclusion of a preload force shows two interesting behaviors. First, the required input force is reduced when $\theta_j$ is between 0 and 90°, but is increased when $\theta_j$ is between 0 and $-90°$.

Second, for $\theta_r = 90^\circ$ the preload force has no effect on the required input force and Eq. 2.7 becomes equivalent to Eq. 2.6.

**Example Design**

To demonstrate the use of these equations, consider a design where the desired jaw rotation is $\pm 90^\circ$ with a jaw length of 6.25 mm and a desired output force of 2 N. Assume that there is not a preload force in the cables. To achieve this motion $\theta_r$ must be at least $45^\circ$. To provide reasonable structural support at the extremes of motion, we will choose $\theta_r = 60^\circ$. The width of the mechanism was chosen to be 2.12 mm such that it fits inside a 3 mm shaft.

The distance from the upper segment to the point of force application ($d_f$) must also be determined (see Fig. 2.2). This distance is defined here as the point where the force would be applied if $\theta_r$ were equal to $90^\circ$. This gives the design the same mechanical advantage as a traditional CORE mechanism, but its overall height is reduced because the actual profile is defined by $\theta_r = 60^\circ$. Therefore, $d_f$ is

$$d_f = r_1(1 - sin_r) = 0.165mm \tag{2.8}$$

The resulting input force, $F_1$, can be determined for any jaw rotation using Eq. 2.6. The value of $\theta_r = 90^\circ$ will be used because that defines the location of force input. For other calculations, such as segment height and range of motion, $\theta_r = 60^\circ$ would be used. Figure 2.4 shows the required input force for a range of $\theta_j$ from $-90^\circ$ to $90^\circ$. This plot shows that the required force is symmetric about $\theta_j = 0$ and ranges between approximately 12 and 16 N. The locations of greatest force are at the extremes of motion. This is to be expected because it is where the moment arm of force application is minimized. A plot of the mechanical advantage, shown in Fig. 2.5, also illustrates this concept where mechanical advantage is maximum at $\theta_j = 0$.

### 2.1.3 Split CORE Cable Conservation

Surgical instruments often employ a pull-pull actuation system where a single DoF is controlled with a pair of complimentary cables [5]. This can be executed by attaching both cables to the same actuator. For cable-length-conservative mechanisms the pair of cables will extend or

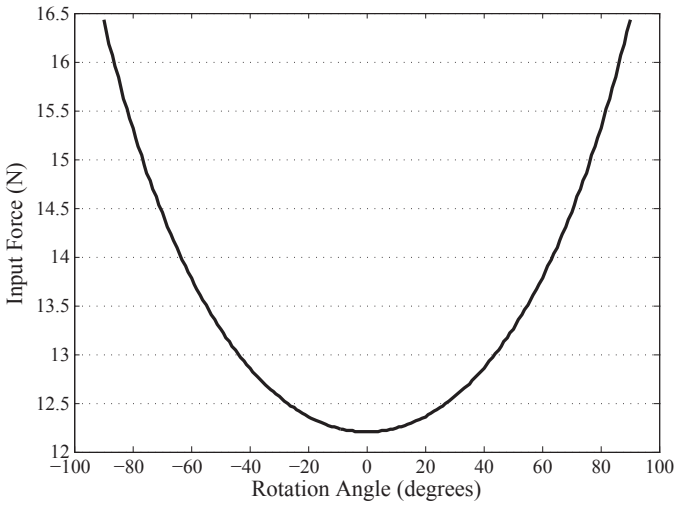


Figure 2.4: The required input force for a Split CORE mechanism with $\pm 90^\circ$ of rotation in $\theta_j$ and an output force of 2 N.

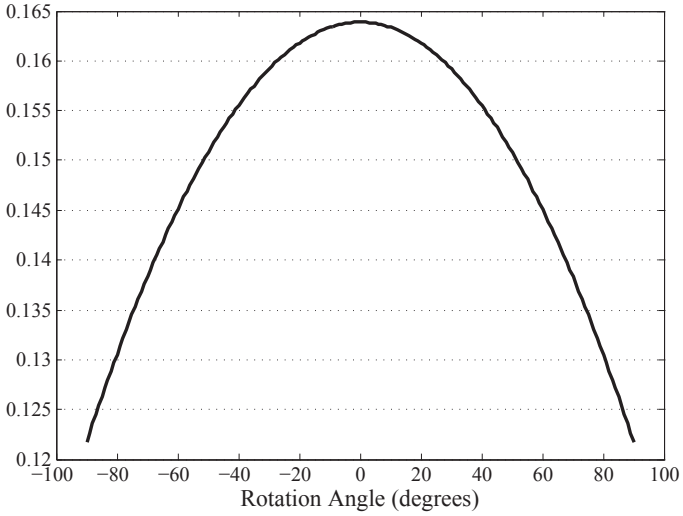


Figure 2.5: The mechanical advantage of an example design for a range of $\theta_j$ from $-90$ to $90^\circ$.

retract the same amount. If the mechanism is non-conservative then the actuating cable will retract less than its companion will extend (or vice versa) resulting in slack and loss of tension on the mechanism. Non-conservative cable lengths also result in increased forces in one of an actuation cable pair as it will stretch to accommodate the difference in length.

A kinematic model shows that cable length is not conservative in the Split CORE joint. The jaws were displaced by $15^\circ$ increments from 0 to $75^\circ$ and the distances between the cable holes

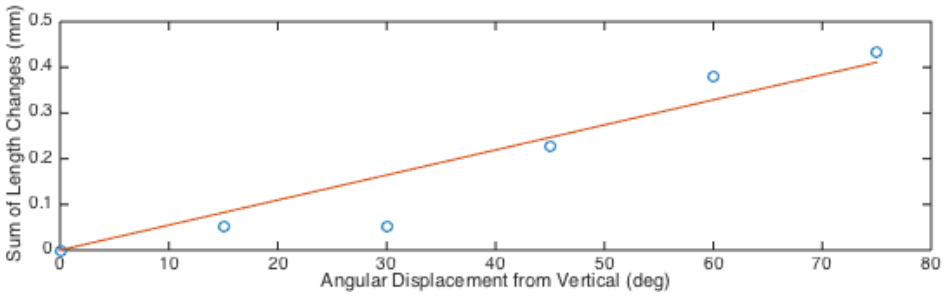


Figure 2.6: The sum of cable length changes for the Split CORE mechanism, illustrating the non-conservative nature of the mechanism

were measured at each increment on both sides of the mechanism. The sum of cable extension and retraction was then plotted as a function of the angular displacement as shown in Fig. 2.6. Length conservative cables would exhibit a horizontal line through the origin.

In the case where the mechanism geometry interrupts the path of the cable, multiple line segments were used to define the length of the cable. The distance from the cable holes to these points on the gear tooth were measured in addition to the line segment extending between the points of interruption. These segments were then summed to estimate the entire relevant cable length.

Figure 2.6 shows that the Split CORE cables are not conservative, but they vary by less than 0.51 mm (0.02 in). Using the force-displacement relationship of the cables, the force required to stretch—and artificially achieve length conservation—can be evaluated. In this case, a force of 6.7 N (1.5 lb) is sufficient. It may also be that 0.51 mm (0.02 in) is sufficiently small to make the non-conservative nature of the cables negligible. Also, this problem could potentially be accommodated by using a separate actuator for each cable or by running the cables over a mirrored mechanism before attaching to the actuators.

## 2.2 Stress Analysis

The most relevant stress states were investigated to evaulate possible failures due to loading.

### 2.2.1 Contact Stress

The critical stresses experienced by the Split CORE mechanism can be estimated using Hertzian Contact Stress Theory [28]. In the case of two circular surfaces, the area of contact forms a rectangle of width $2b$ and length $l$, where $l$ is the total length of the flat regions carrying the compressive loads (refer to Fig. 2.3) and

$$b = \sqrt{\frac{4r_1 F\left(1-\nu^2\right)}{\pi l E}} \tag{2.9}$$

where $F$ is the input force $F_1$ or $F_2$, depending on which case is being considered, $\nu$ is Poisson's ratio, and $E$ is the modulus of elasticity for the material being used. Equation 2.9 assumes that the radius of curvature for upper and lower segments are equal and that both are of the same material.

The contact area creates an elliptical pressure distribution with its maximum at the center. The maximum pressure is defined as

$$P_{max} = \frac{2F}{\pi b l} \tag{2.10}$$

Subsequently, the stress states along each of the three axes can be expressed in terms of the distance away from the point of contact, or the depth into the material, denoted as $y$. These expressions are given by

$$\sigma_x = -P_{max}\left(\frac{1+2\left(\frac{y}{b}\right)^2}{\sqrt{1+\left(\frac{y}{b}\right)^2}} - \left|\frac{y}{b}\right|\right) \tag{2.11}$$

$$\sigma_y = \frac{-P_{max}}{\sqrt{1+\left(\frac{y}{b}\right)^2}} \tag{2.12}$$

$$\sigma_z = -2\nu P_{max}\left(\sqrt{1+\left(\frac{y}{b}\right)^2} + \left|\frac{y}{b}\right|\right) \tag{2.13}$$

**Example Design**

This example uses parameters found in the previous example and titanium (Ti-6Al-4V) with an elastic modulus of 114 GPa, compressive yield strength of 1070 Mpa, and Poisson's ratio

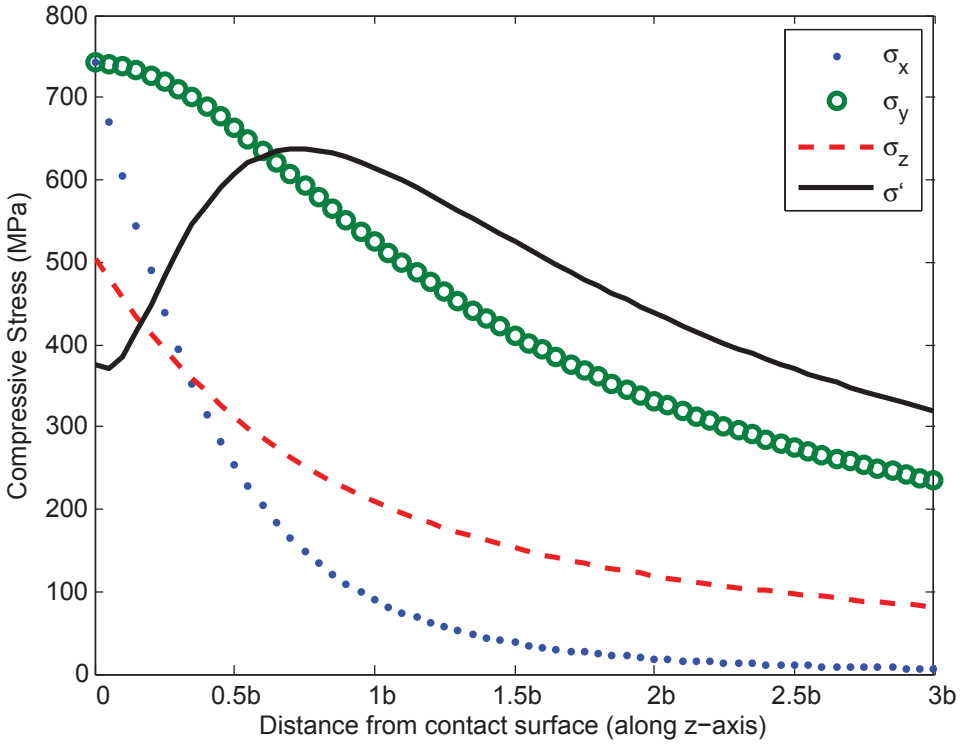


Figure 2.7: Principal and von Mises Stresses as a function of the distance from the contact surface

of 0.34. The non-geared portion of the contact surface (see Fig. 2.3) is chosen to be one third of the total length of the joint, where the length of the joint is equal to $2r_1$, or 2.12 mm, so that it fits on a 3 mm instrument shaft. $l$ is calculated to be approximately 0.7 mm and Eq. 2.9 is used to find $b = 0.015$ mm. These calculations are based on the position at which $\theta_j = 0$, which corresponds to $F_1 = 12.2$ N but, this same approach applies at any angle of rotation.

These values are substituted into Eq. 2.10 to calculate a contact pressure of $P_{max} = 742$ MPa. Equations 2.11-2.13 are used to determine each of the stress states shown in Fig. 2.7. The maximum stress in each of the three directions occurs at the outer surface where contact is made. The maximum stresses for $\sigma_x$, $\sigma_y$, and $\sigma_z$ at this location are 742 MPa, 742 MPa, and 504 Mpa, respectively. This results in a maximum Von Mises stress of $\sigma' = 638$ MPa. The location of the maximum Von Mises stress is approximately 0.011 mm from the contact surface ($z \approx 0.74b$) and represents a minimum safety factor of 1.68.

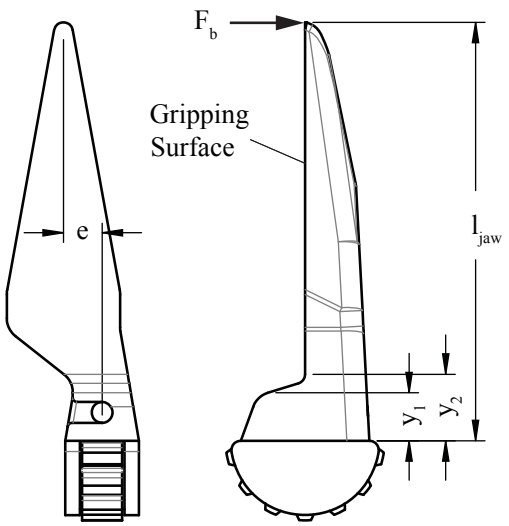


Figure 2.8: Parameters used in bending stress analysis

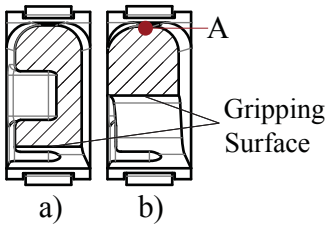


Figure 2.9: Top view of the two smallest cross sections located ata a) $Y_1$ and b) $Y_2$ (see Fig. 2.8). The maximum bending stress occurs at point A in section B.

### 2.2.2 Bending Stress

The two smallest cross sections located the farthest away from the applied load were identified and analyzed. These cross sections are located distances $y_1$ and $y_2$ from the cantilevered face (see Fig. 2.8). The applied load acts through a moment arm $l_i = l_{jaw} - y_i$. The stress due to bending as well as the torsional stress resulting from the eccentric loading were calculated using the equations $\sigma = \frac{Mc}{I}$ and $\tau = \frac{Tc}{J}$, where $M = FL_i$ and $T = F_b e$.

The maximum stress in the jaw occurs at point A on cross section b (Fig. 2.9b). The Von Mises stress is 306.1 MPa which represents a factor of safety of 3.5.

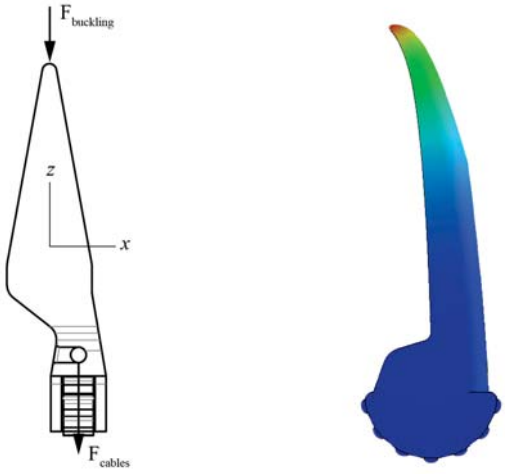


(a) Parameters used in buckling analysis

(b) Shape of 1st mode of buckling

Figure 2.10: Buckling analysis

### 2.2.3 Buckling

An FE model and a simplified analytical model were evaluated to determine the likelihood of buckling due an applied axial load (see Fig. 2.10(a)). The FE model was constrained in the $x$ and $y$ directions by limiting the movement of the center gear tooth and similarly constrained in the $z$ direction by fixing the translation of the rolling contact surface. Additionally, the preload forces from the cables ($F_{cables} = 11.1\ N$) were applied on either end of the through hole.

Under these conditions, with an axial force of $F_{buckling} = 133.4$ N. the minimum factor of safety was 1.94. The shape of the first mode of buckling can be seen in Fig. 2.10(b).

### 2.2.4 Stress Analysis Results

Because the loads to failure in the stress states are much higher than the expected required output forces, it appears that failure due to stresses in the structural members of the instrument is unlikely. Alternative failure modes that better define the limitations of the design, like joint disengagement, are discussed next.

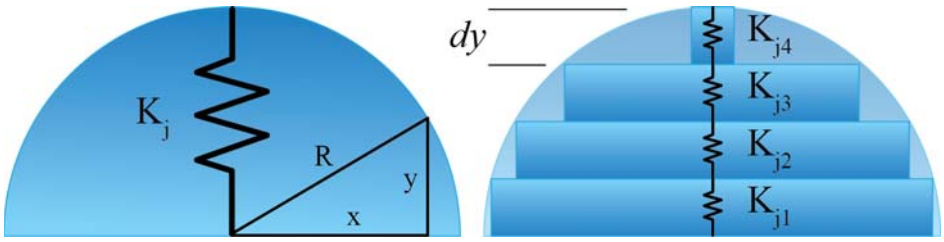


Figure 2.11: Stiffness of a half cylinder

## 2.3 Disengagement

The Split CORE is held together with tension from its actuation cables. Although it simplifies assembly, it also represents potential risks if the mechanism were to disengage during use. The following sections address the most likely disengagement scenarios.

### 2.3.1 Axial Disengagement

The Split CORE joint consists of two mating half cylinders held together in compression by two actuator cables. Both the cables and the joints were modeled as springs to determine the force required to extend the cables to 50% engagement of the gearing.

Figure 2.11 shows a half cylinder discretized into sections, each with their own spring constants. These can be treated as springs in series and evaluated to estimate the entire stiffness of the joint $K_j$. As the height of each cross-section $dy$ is decreased, the summation of the spring constants can be evaluated in the form of an integral. This yields a joint stiffness of $K_j = \frac{4lE}{\pi}$ where $l$ is the length of the rolling contact areas (as viewed into the page), and $E$ is the modulus of the material.

Figure 2.12 illustrates how this spring constant can be used to construct a series of springs representative of the joint. The two half cylinders ($K_j$) act as springs in series while the cables ($K_c$) act as springs in parallel. The value of $K_c$ was obtained through testing of the cabling used in prototypes. The cables and joint act as springs in series because for a given force they will not undergo the same deflection.

The equivalent spring constants of the joint and cables are used to determine the value of $F_a$ required for 50% engagement. $F_c$, the tensioning force on the cables before $F_a$ is applied, will

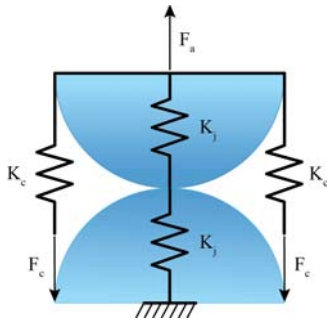


Figure 2.12: Split CORE as a system of springs

initially cause the joint to compress. It follows that $F_a$ is the force required to first release the compression in the joint and stretch the cables 0.04 mm (half the distance from the contact surface to the tip of the gear teeth). Subsequently, calculating $F_a$ is simple:

$$F_a = 2K_c(\delta_j + \delta_{50}) = 3.9\ N \tag{2.14}$$

where $2K_c$ is the equivalent spring constant of the two cables, $\delta_J = \frac{4F_c}{K_J}$ is the original deflection of the joint and $\delta_{50}$ is the distance from the rolling contact surface to 50% gear tooth engagement.

For the geometry of the example $F_a = 3.9\ N$. While this is not a large magnitude force, it may be appropriate for such a small mechanism. The predicted output forces for the Split CORE are on the same order of magnitude and many of the motions used by surgeons are rarely purely axial translation. Any lateral motion of the joint will have the added benefit of the mechanical constraints imposed by the gearing in addition to the stiffness of the cables to keep the joint engaged.

### 2.3.2 Lateral Tipping

The force required to tip the jaws off the top of the mechanisms, $F_{tip}$, is also of interest (see Fig. 2.13). This force was calculated for three separate configurations.

1. The original design with no side walls
2. Side walls added for additional stability
3. Friction forces resulting from the cable pre-loading taken into consideration

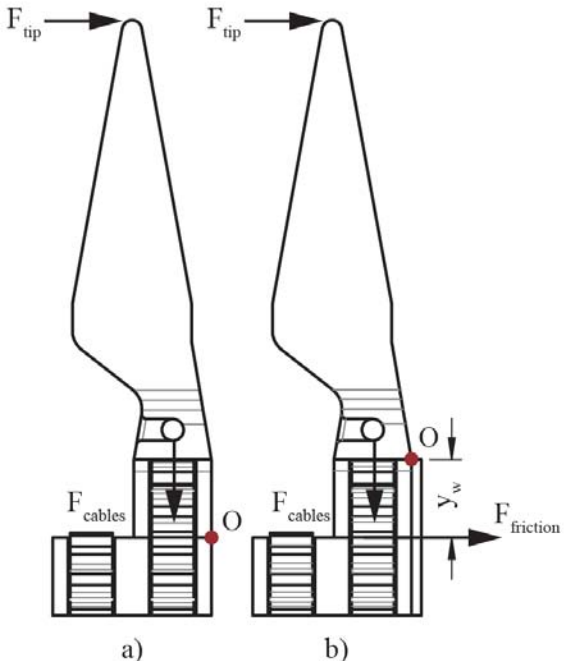


Figure 2.13: Configurations used in lateral tipping analysis

The moments resulting from $F_{tip}$ and $F_{cables}$ were balanced around point $O$ shown in Fig. 2.13. The friction force $F_{friction} = 2F_{cables}\mu$ where $\mu$ is the coefficient of friction, was added to the moment balance equation for scenario 3. The dynamic coefficient of friction for steel on steel was used in place of the static coefficient as a conservative approximation. The equations for the three configurations are as follows:

$$F_{tip1} = \frac{2F_{cables}x_c}{l_{jaw}} \tag{2.15}$$

$$F_{tip2} = \frac{2F_{cables}x_c}{l_{jaw} - y_w} \tag{2.16}$$

$$F_{tip3} = \frac{2F_{cables}(x_c + \mu y_w)}{l_{jaw} - y_w} \tag{2.17}$$

The results for the example mechanism are summarized in Table 2.1.

Table 2.1: Tipping force for 3 scenarios

| Scenario | Load (N) |
|---|---|
| 1 | 2.0 |
| 2 | 2.4 |
| 3 | 5.3 |

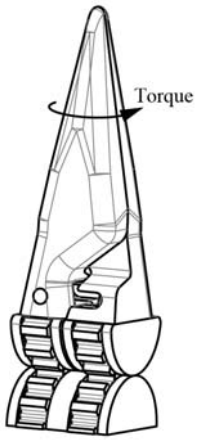


Figure 2.14: Parameters used in torque analysis

### 2.3.3 Torsional Disengagement

Four variations on the Split CORE design were subjected to an axially applied torque (Fig. 2.14) to compare their resistance to torsional disengagement. Testing was completed at five times scale. The four variations include the a) original, b) outer walled, c) low three-walled, and d) high three-walled designs illustrated in Fig. 2.15. The three-walled design yielded the greatest improvement over the original by carrying 23.5% more torque before failure.

A fixture was designed and built to create a repeatable test. The joint was held in compression with a cord to mimic the loading in the final instrument. The cable tension was scaled up four times (44.5 N or 10 lb) to approximate the scale of the mechanism itself. Custom printed joints (shown in Fig. 2.16b) included a moment arm where additional weights were attached to simulate an applied torque along the axis of the instrument (Fig. 2.16c). The cables attaching the weights to

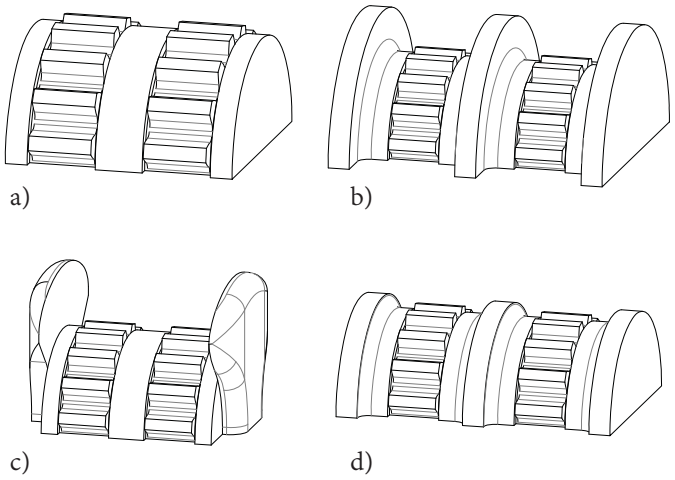


Figure 2.15: Four design variants used in comparative torsional analysis a) original b) outer walled c) low three-walled d) high three-walled

Table 2.2: Torque to failure and standard deviation for four design variants

| Variant | Torque to Failure (N·m) | $\sigma$ |
|---|---|---|
| a | 0.24 | 0.71 |
| b | 0.29 | 0.10 |
| c | 0.28 | 0.71 |
| d | 0.32 | 0.27 |

the joint were routed over a low friction pulley to ensure the load was transferred to the joint with negligible frictional losses. The torque was increased by 9.5 N·mm by adding 100 g increments until the joint derailed or the parts failed. This was repeated five times for each of the four design types in a random order to help normalize operator error and bias.

The test results listed in Table 2.2 show that any mechanical features constraining the parts in torsion add considerable stability to the design. It is not surprising that the high three-walled design provides the greatest improvement with a 23.5% increase in load capacity. However, it is somewhat unexpected that the outer walled and low three-walled variations provide similar in-

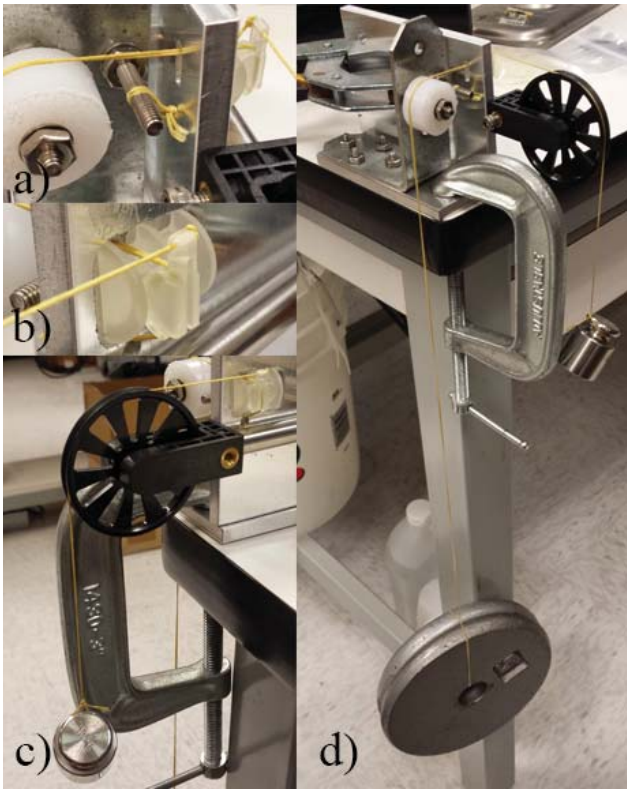


Figure 2.16: Test fixture used to test design variants A) cable holding joints in compression B) custom 3D printed joints with moment arm C) weight applying torsional load D) weight keeping joint in compression

creases in stability at 15.3% and 14.2%, respectively. Because the outer walled design was tested with one jaw in place, it is likely that with both jaws engaged, the performance would improve even further. The second jaw would likely add increased resistance to torsion.

The second and fourth design also exhibited less variation in their performance. Table 2.2 lists the average torque value before failure for each design variation. Additionally, it includes the standard deviation for the sample set. Designs 1 and 3 both had $\sigma = 0.71$ while designs 2 and 4 had $\sigma = 0.10$ and 0.27 respectively.

Figure 2.17: Comparison of existing (8.4 and 5.5 mm) and prototype (4.1 mm) surgical instruments next to a U.S. penny

## 2.4 Testing

### 2.4.1 Assembly

A collar surrounding the jaws provides increased stability against both torsional and lateral forces. An existing wrist mechanism designed by Intuitive Surgical, Inc. was added beneath the Split CORE joint to achieve a third DoF.

### 2.4.2 Polymer Prototypes

Several proof-of-concept prototypes were made from Fused Deposition Modeled (FDM) polymers. A 10X scale model was created to show the general feasibility of the design. To demonstrate that the mechanism could be controlled by a robotic system, a scale prototype was built with Stereolithography (SLA) and integrated with existing instrument architectures. Basic manipulation of the mechanism was achieved using a *Da Vinci* surgical robotic system. The fundamental motions required for suturing were demonstrated, although the usefulness of the prototype was limited by the strength of the prototype polymer material.

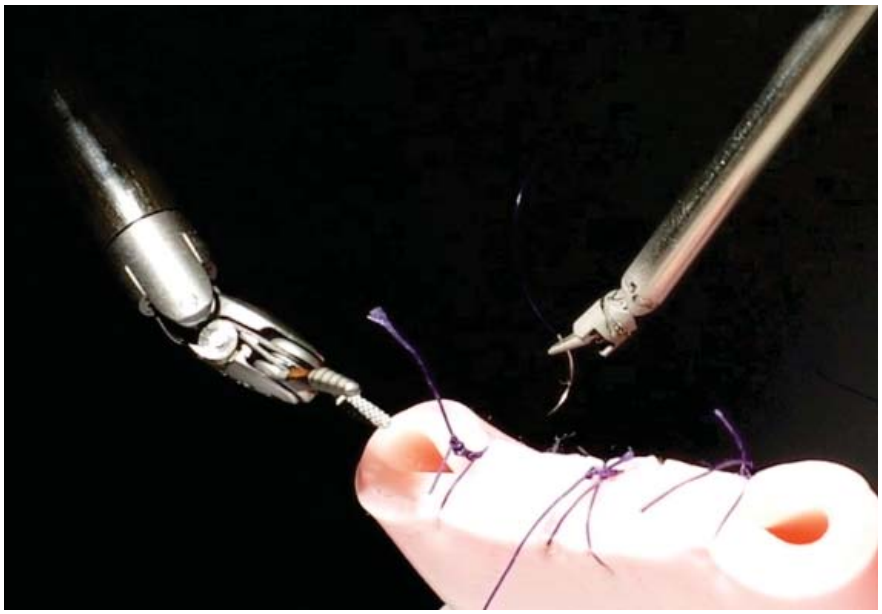

Figure 2.18: Robotically actuated Split CORE prototype (on the right) driving a 7-0 suture (on the left is an 8.4 mm instrument for comparison)

### 2.4.3 Stainless Steel Prototypes

Traditional methods would be at the edge of their limits to create the features at the required definition for smooth engagement and performance. As a result, a micro Metal Laser Sintering (MLS) method was used to create the first metal prototypes.

This method is similar to existing MLS methods. Fine metal powders with an average particle size distribution of $< 5\mu m$ D90 (at least 90% of the particles are less than 5 $\mu m$ in diameter) are used. This allows the build to achieve tolerances on the order of $\pm 5\mu m$ and features as small as $25\mu m$. These capabilities represent a great improvement over traditional machining or Metal Injection Molding (MIM) methods that typically have difficulty accurately defining features much smaller than $100\mu m$.

The result of this method is a well defined, working prototype shown in Fig. 2.17. The metal used is 316L Stainless Steel with a demonstrated tensile strength of 694 MPa.

Figure 2.18 shows an assembled prototype on the right in the process of suturing next to a 8.4 mm instrument. It is being robotically controlled by a *Da Vinci* surgical robot. The prototype

demonstrated the dexterity and strength required to repeatedly drive the suture through the foam and pass the suture back and forth between the adjacent instrument.

## 2.5 Conclusion

Equations have been developed for analyzing the design's force-deflection behavior, stress, and resistance to disengagement. Tests have been conducted to evaluate torsional disengagement, and a physical prototype has been fabricated and tested to demonstrate feasibility and compatibility with existing robotic surgical systems.

The physical prototype is 4.1 mm in diameter with 3 DoF at the distal end. Additionally the wrist is only 5.4 mm long. This represents a 25.5% reduction in instrument diameter and a 74.1% reduction in joint length over commercially available alternatives. The reduction in joint length in addition to well contained centers of rotation result in a drastically reduced swept volume. This means that the volume required for the instrument to operate has been reduced and the instrument can operate in cavities previously too small or restricting for existing instruments.

The result of this design is a novel 3 DoF gripping mechanism with only 6 total parts, 4 of which are unique. 2 DoFs are inherent to the Split CORE design and a third DoF was added by combining with an existing wrist design provided by Intuitive Surgical Inc. The design is achieved within a 4.1 mm diameter. The production methods used enable even further scaling, creating the potential for instruments on the order of 2 to 3 mm in diameter. The mechanism has demonstrated force outputs large enough that it could prove useful in suturing or other surgical tasks.

## CHAPTER 3. THE CROSSED CYLINDERS WRIST

The goal for this mechanism is to condense a wrist-like motion, or two Degrees of Freedom (DoF), into a compact structure with the fewest number of parts possible. Additionally, it is desirable to have a mechanisms that travels through its full range of motion in a relatively small volume while only requiring simple assembly. The presented mechanism fulfills both of these requirements.

The crossed cylinders wrist integrates two half-cylinders whose longitudinal axes are offset by 90°. The surfaces of the half cylinders have been populated with gearing that enables the two halves to roll in two directions while preventing slip. This is achieved by using involute gear profiles along the curvature of the half-cylinders and a rack profile along the axis of the cylinders. Every other row of gearing is offset by half the circular pitch of the involute gearing to increase the number of gear teeth that are engaged at any instant. A 3D printed proof of concept prototype is shown in Fig. 3.1.

Figure 3.1: 3D printed prototype showing two half-cylinders that mesh with each other by means of bi-directional gearing

The two halves are not identical but are the mirror of each other so they will be centered when interfacing. This effect is a function of the 90° offset. When rolling purely along the axis of

the bottom half of the joint (the base), the top half (the platform) rolls like a wheel. This causes the center of the platform to remain at the same relative elevation. Conversely, when the platform rolls along the curvature of the base, it is as if a rectangle is being rolled over a half circle. This motion will be explored in more detail in later sections.

## 3.1 Advantages

The crossed cylinders have a few distinct advantages over the myriad of two Degree of Freedom (DoF) joints that currently exist. The advantages stem from several main features of the joint:

1. Rolling contact
2. Positive engagement
3. Low part count and self assembly
4. Compact motion

There is little friction between the two halves because they roll across one another with little relative motion. Binding, a limiting factor in many mesoscale designs caused by friction, is attenuated by this rolling motion. Low friction between joint parts eliminates the need for lubricant.

The gearing between the two halves of the joint ensures that there is effectively no slip, leading to a positive engagement design. This means that there is a predictable relationship between an input motion or force and the resulting output motion or force.

The design is simple enough that it can potentially be produced at mesoscale and still function properly. Fabrication has been demonstrated using a layered Carbon Nanotube (CNT) method and similar designs have been produced using micro Metal Laser Sintering 3D printing methods [29]. Once the parts are made and put in place, they remain in contact through the forces imposed by the actuation cables.

The wrist has only two parts to achieve two DoFs. Both centers of rotation for each DoF, although non-constant, remain somewhere in between the two parts through their range of motion. This results in the mechanism only using a small volume through its range of motion.

## 3.2 Challenges

The mechanism is not without its challenges. The most significant of these challenges are listed below.

1. Variable center of rotation
2. Fabrication of 3D geometry at mesoscale
3. Oblique loading
4. Actuation cable routing

The rolling motion of the two halves of the wrist result in a variable center of rotation for each degree of freedom. This is a challenge when describing the motion of the mechanism. However, the challenge is addressed through a kinematic analysis of the mechanism that predicts the position of any point relative to the mechanism platform through its range of motion.

The bi-directional gear profiles (to be discussed in the following section) result in complex 3D structures to produce at scale with traditional manufacturing methods. They have been prototyped using several alternative methods described in Chapter 4. This geometry also poses a challenge in analyzing the loads on the mechanism. An basic approach is taken analyzing the gear teeth in compression and bending to find the loads to failure.

The cable routing is also a challenge because it has an impact on the mechanical advantage of the mechanism. Feasibility is shown with a large scale prototype but future work on the mechanism could take a detailed approach to overcoming this particular hurdle.

## 3.3 Gear Profiles

The crossed cylinders wrist employs two different gear profiles because of the differing cross sections. A cross section on a plane perpendicular to the axis of the cylinder is a half circle. An involute profile is used here as shown on the left side of Fig. 3.2. Conversely, a cross section along the axis of the cylinder is a rectangle. An involute profile is similarly applied and becomes a rack profile, as shown on the right of Fig. 3.2, due to the infinite radius of curvature.

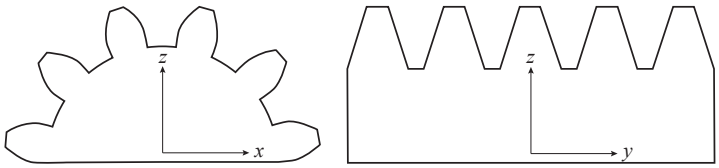


Figure 3.2: Involute and rack profiles

The novelty of the cross cylinders wrist comes with combining both profiles on the same tooth. Each tooth incorporates both geometries such that no matter how the joint is displaced ($\pm 90^\circ$ in two orthogonal directions), it will have teeth engaged to prevent it from slipping. Thus each tooth becomes a pseudo-pyramid shape with a trapezoidal rack profile on two opposite sides, and the involute profile on the other sides.

The tooth width is half the circular pitch, $p = \frac{\pi}{D_p}$, or $w_t = \frac{p}{2}$, where $D_p$ is the diametral pitch. Every other row of teeth along the axis of the cylinder is separated by a distance of $w_t$. Additionally, each adjacent row of teeth is rotated by $\frac{360}{2N}$ degrees so that when a given tooth is engaged it is surrounded on all sides by mating teeth.

### 3.4 Kinematics

The kinematics of the mechanism is described by two vectors. The first vector, $\mathbf{r_p}$, from the origin $O$ to the center of the platform surface at point $P$ and the second, $\mathbf{r}_{*/\mathbf{P}}$, from $P$ to some arbitrary point of interest $*$ as shown in Fig. 3.3. The vector $\mathbf{r_p}$ was derived by considering the 2D motion in the $x-z$ and $y-z$ planes separately. It can be shown that the elevation of the point $P$ only depends on $\theta_1$ (an angular displacement in the $x-z$ plane). This is because when the joint is displaced by $\theta_2$ (the angular displacement in the $y-z$ plane) the point $P$ acts like the center of a wheel and will only translate horizontally in the plane. These angles are shown in Fig. 3.4. Using this information the two separate expressions can be joined to define $\mathbf{r_p}$ as

$$\mathbf{r_p} = [(r_1+r_2)\,sin\theta_1 - r_1\theta_1 cos\theta_1]\,\hat{\mathbf{i}} - r_2\theta_2\hat{\mathbf{j}} + [(r_1+r_2)\,cos\theta_1 + r_1\theta_1 sin\theta_1]\,\hat{\mathbf{k}} \tag{3.1}$$

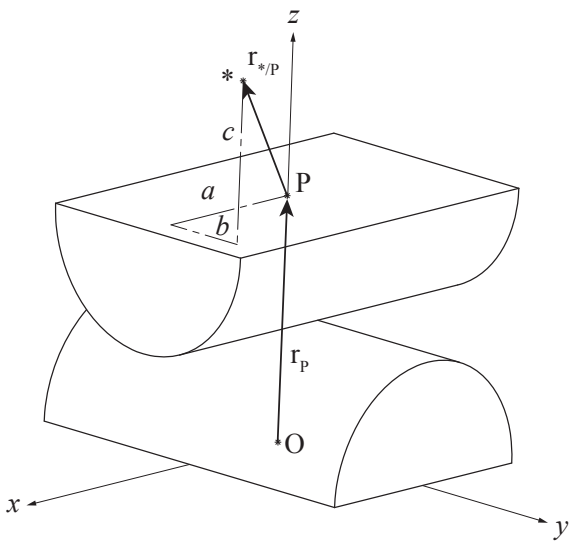


Figure 3.3: The vectors used to describe the kinematics of the crossed cylinders wrist

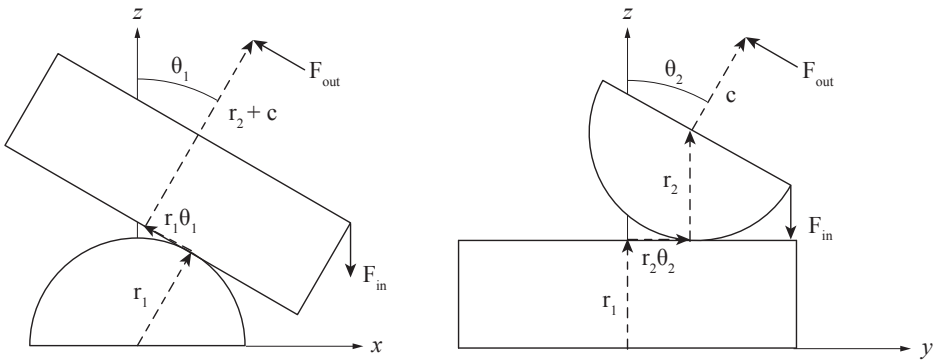


Figure 3.4: Planar views of the crossed cylinders wrist. Left: $x-z$ plane is dependant on $\theta_1$ Right: The $y-z$ plane is dependant on $\theta_2$

The motion of this point traces out a surface that can be seen in Fig. 3.5(a).

The vector $\mathbf{r}'_{*/\mathbf{P}}$ is best described using a body-fixed frame with its origin attached to point $P$. Vectors expressed in this rotating frame will be indicated by a prime symbol $'$. The vector from $P$ to $*$ expressed in the new coordinate frame is therefore

$$\mathbf{r}'_{*/\mathbf{P}} = a\,\hat{\mathbf{i}}' + b\,\hat{\mathbf{j}}' + c\,\hat{\mathbf{k}}' \tag{3.2}$$

When the joint is undeflected, or $\theta_1 = \theta_2 = 0$, the rotating frame is lined up with the global coordinate system. For any given position, the rotating frame can be thought to go through some initial rotation about the $y$ axis followed by another rotation about its new $x$ axis. These rotations correspond to $\theta_1$ and $\theta_2$ respectively. Therefore, to transform $\mathbf{r}'_{*/\mathbf{P}}$ into the global coordinate frame, two rotation matrices

$$[\mathbf{R_y}] = \begin{bmatrix} cos\theta_1 & 0 & -sin\theta_1 \\ 0 & 1 & 0 \\ sin\theta_1 & 0 & cos\theta_1 \end{bmatrix} \tag{3.3}$$

and

$$[\mathbf{R_x}] = \begin{bmatrix} 1 & 0 & 0 \\ 0 & cos\theta_2 & sin\theta_2 \\ 0 & -sin\theta_2 & cos\theta_2 \end{bmatrix} \tag{3.4}$$

can be multiplied to express a single rotation matrix transforming vectors from the global coordinate frame into the rotating frame as

$$[\mathbf{R}] = [\mathbf{R_x}]\,[\mathbf{R_y}] = \begin{bmatrix} cos\theta_1 & 0 & -sin\theta_1 \\ sin\theta_1 sin\theta_2 & cos\theta_1 & cos\theta_1 sin\theta_2 \\ sin\theta_1 cos\theta_2 & -sin\theta_2 & cos\theta_1 cos\theta_2 \end{bmatrix} \tag{3.5}$$

Conversely, the transformation from the rotating frame back in to the global coordinate system can be achieved by using the transposed rotation matrix $[\mathbf{R}]^T$

$$[\mathbf{R}]^T = \begin{bmatrix} cos\theta_1 & sin\theta_1 sin\theta_2 & sin\theta_1 cos\theta_2 \\ 0 & cos\theta_1 & -sin\theta_2 \\ -sin\theta_1 & cos\theta_1 sin\theta_2 & cos\theta_1 cos\theta_2 \end{bmatrix} \tag{3.6}$$

to modify a vector of interest. Using this method $\mathbf{r}'_{*/\mathbf{P}}$ (Fig. 3.3) can be transformed into the global coordinate system by the expression $\mathbf{r}_{*/\mathbf{P}} = \mathbf{R}^T \mathbf{r}'_{*/\mathbf{P}}$. This yields

$$\mathbf{r}_{*/\mathbf{P}} = (a\cos\theta_1 + b\sin\theta_1\sin\theta_2 + c\sin\theta_1\cos\theta_2)\,\hat{\mathbf{i}} + (b\cos\theta_2 - c\sin\theta_2)\,\hat{\mathbf{j}} + (-a\sin\theta_1 + b\cos\theta_1\sin\theta_2 + c\cos\theta_2\cos\theta_2)\,\hat{\mathbf{k}} \quad (3.7)$$

The total vector from the origin to point $*$ is now just a matter of vector addition where $\mathbf{r}_* = \mathbf{r}_\mathbf{P} + \mathbf{r}_{*/\mathbf{P}}$.

$$\begin{aligned}\mathbf{r}_* = {} & [(r_1 + r_2)\sin\theta_1 + (a - r_1\theta_1)\cos\theta_1 + b\sin\theta_1\sin\theta_2 + c\sin\theta_1\cos\theta_2]\,\hat{\mathbf{i}} \\ & + [b\cos\theta_2 - c\sin\theta_2 - r_2\theta_2]\,\hat{\mathbf{j}} \\ & + [(r_1 + r_2)\cos\theta_1 + (r_1\theta_1 - a)\sin\theta_1 + b\cos\theta_1\sin\theta_2 + c\cos\theta_2\cos\theta_2]\,\hat{\mathbf{k}}\end{aligned} \quad (3.8)$$

This expression can generate surfaces traced by any point fixed to the platform. For example, if a gripper of length equal to a unit radius were fixed to the platform, it would trace out a surface with the same shape shown in Fig. 3.5(b). The somewhat elliptical surface is a product of the non-constant center of rotation. As the distance above the surface of the platform increases the surface will take on a more spherical shape because while the effective radius is increasing the change in center of rotation remains constant.

## 3.5 Mechanical Advantage

The expression given in Eq. 3.8 can be modified to give the location of any point fixed to the platform. This is useful when determining the relationship between input and output forces. The motion of the crossed cylinders wrist can be expressed in two orthogonal directions. To simplify initial calculations, the mechanical advantage was initially derived for two planar cases.

### The $x-z$ Plane

The principle of virtual work can be applied to a simplified planar model of the crossed cylinders wrist to develop an expression for the mechanical advantage. Figure 3.4 shows the pa-

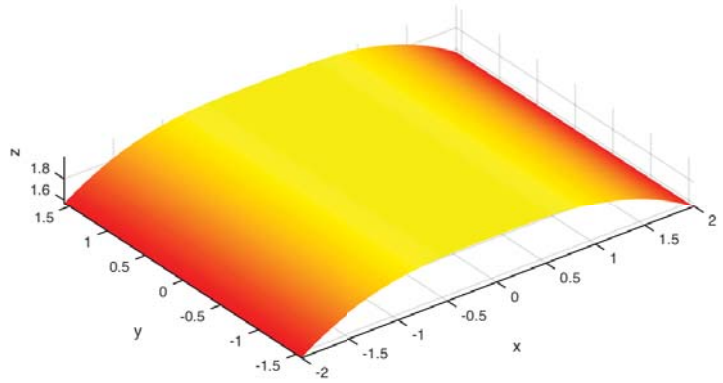


(a) Surface traced by point $P$

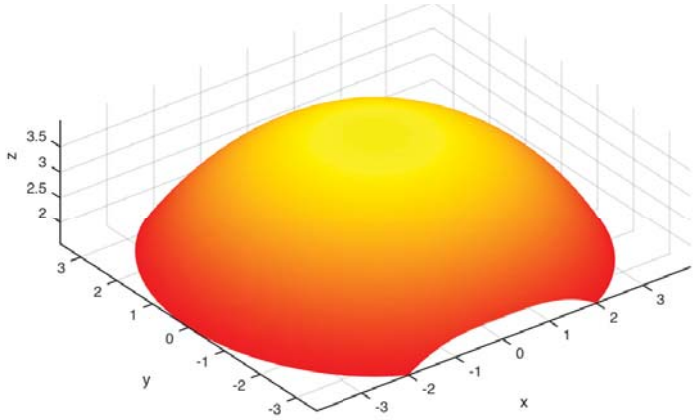


(b) Surface traced by point $*$ ($a$ and $b = 0$, $c = 1$)

Figure 3.5: Surfaces traced by points $P$ and $*$ as $\theta_1$ and $\theta_2$ vary from $\pm 90^\circ$

rameters used in the following derivation. An input force applied at the top right corner, or a magnitude of $a$ away from point $P$ is assumed to always act vertically downward.

$$\mathbf{F_{in}} = -F_{in}\hat{k} \tag{3.9}$$

An apposing follower force, modeling some output force, is applied a distance $c$ above the center of the platform as expressed in Eq. 3.10.

$$\mathbf{F_{out}} = F_{out}\left(-\cos\theta_1\hat{\mathbf{i}} + \sin\theta_1\hat{\mathbf{k}}\right) \tag{3.10}$$

The position vectors to the input and output forces are expressed in Eqs. 3.11 and 3.12 respectively.

$$\mathbf{r_{in}} = [(r_1 + r_2)\sin\theta_1 + (a - r_1\theta_1)\cos\theta_1]\,\hat{\mathbf{i}} + [(r_1 + r_2)\cos\theta_1 + (r_1\theta_1 - a)\sin\theta_1]\,\hat{\mathbf{k}} \tag{3.11}$$

$$\mathbf{r_{out}} = [(r_1 + r_2 + c)\sin\theta_1 + r_1\theta_1\cos\theta_1]\,\hat{\mathbf{i}} + [(r_1 + r_2 + c)\cos\theta_1 + r_1\theta_1\sin\theta_1]\,\hat{\mathbf{k}} \tag{3.12}$$

Taking the derivatives of the position vectors with respect to the generalized coordinate and simplifying, the virtual displacements become:

$$\delta\mathbf{r_{in}} = \left\{[r_2\cos\theta_1 - a\sin\theta_1 + r_1\theta_1\sin\theta_1]\,\hat{\mathbf{i}} + [-r_2\sin\theta_1 + r_1\theta_1\cos\theta_1 - a\cos\theta_1]\,\hat{\mathbf{k}}\right\}\delta\theta_1 \tag{3.13}$$

$$\delta\mathbf{r_{out}} = \left\{[(r_2 + c)\cos\theta_1 + r_1\theta_1\sin\theta_1]\,\hat{\mathbf{i}} + [-(r_2 + c)\sin\theta_1 + r_1\theta_1\cos\theta_1]\,\hat{\mathbf{k}}\right\}\delta\theta_1 \tag{3.14}$$

The virtual work for each applied force is simply the dot product of each applied force with its corresponding virtual displacement. $\delta\mathbf{W_i} = \mathbf{F_i}\cdot\delta\mathbf{r_i}$ Therefore $\delta\mathbf{W_{in}}$ is expressed in Eq. 3.15

$$\delta\mathbf{W_{in}} = -F_{in}\,[-r_2\sin\theta_1 + r_1\theta_1\cos\theta_1 - a\cos\theta_1]\,\delta\theta_1 \tag{3.15}$$

Interestingly, the expression for $\delta\mathbf{W_{out}}$ can be simplified trigonometricaly until it becomes Eq. 3.16

$$\delta\mathbf{W_{out}} = -F_{out}\,(r_2 + c)\,\delta\theta_1 \tag{3.16}$$

The sum of these virtual work terms is the total virtual work for the system and is equal to 0 because the system is in equilibrium. Carrying out this summation and rearranging terms, the mechanical advantage, or the ratio $\frac{F_{out}}{F_{in}}$, is

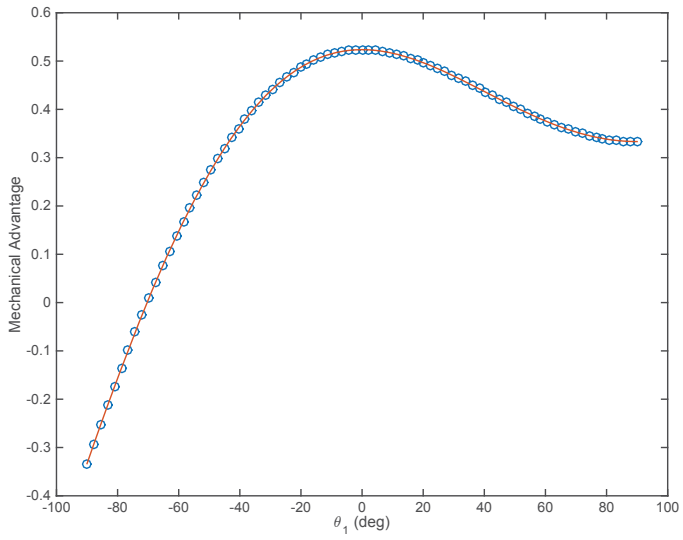


(a) Mechanical advantage in the $x-z$ plane with a max value of 0.5 and zero value at $-70^\circ$

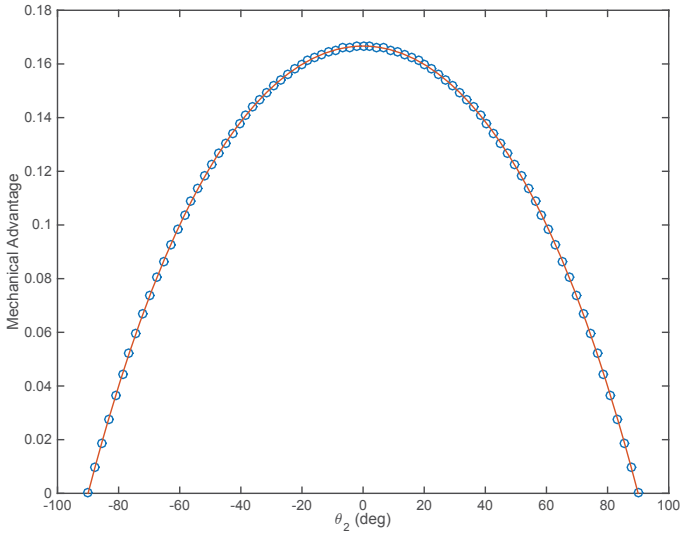


(b) The mechanical advantage in the $y-z$ plane. Max value of 0.17 and zeros at $\pm 90^\circ$.

Figure 3.6: Comparison of two methods for deriving the mechanical advantage in two orthogonal planes. Circles and the line represent the 2D and 3D derivations respectively.

$$\frac{F_{out}}{F_{in}} = \frac{(a - r_1\theta_1)\cos\theta_1 + r_2\sin\theta_1}{r_2 + c} \tag{3.17}$$

As a check, this planar case was compared with an equivalent system based on the 3D kinematic model derived in Eq. 3.8. The result is plotted in Fig. 3.6(a).

Note that the mechanical advantage passes through zero. This occurs when the input force passes directly over the point of contact at approximately $-60^\circ$.

### 3.5.1 The $y-z$ Plane

The same process can be followed to derive an expression for the mechanical advantage in the $y-z$ plane. The 3D position equations developed in Eq. 3.8 will be used here to demonstrate the method used previously.

The same vector describing the input force as expressed in Eq. 3.9 can be reused here. The output force, $\mathbf{F_{out}}'$, however is modeled as a follower force in the rotating coordinate frame.

$$\mathbf{F_{out}}' = -F_{out}\hat{\mathbf{j}}' \tag{3.18}$$

This vector can then be transformed into the global coordinate frame

$$[\mathbf{R}]^T\,\mathbf{F_{out}}' = -F_{out}\left(\sin\theta_1\sin\theta_2\hat{\mathbf{i}} + \cos\theta_2\hat{\mathbf{j}} + \cos\theta_1\sin\theta_2\hat{\mathbf{k}}\right) \tag{3.19}$$

The rest of the process follows the same steps taken in the previous section but with the initial position vectors derived from Eq. 3.8. Accordingly, the location of the input force contains no $a$ or $c$ component, and is expressed as Eq. 3.20

$$\begin{aligned}\mathbf{r_{in}} = {} & [(r_1+r_2)\sin\theta_1 - r_1\theta_1\cos\theta_1 + b\sin\theta_1\sin\theta_2]\,\hat{\mathbf{i}} \\ & + [-r_2\theta_2 + b\cos\theta_2]\,\hat{\mathbf{j}} + [(r_1+r_2)\cos\theta_1 + r_1\theta_1\sin\theta_1 + b\cos\theta_1\sin\theta_2]\,\hat{\mathbf{k}}\end{aligned} \tag{3.20}$$

Similarly, the vector to the output force has no component of $a$ or $b$ in it.

$$\begin{aligned}\mathbf{r_{out}} = {} & [(r_1+r_2)\sin\theta_1 + r_1\theta_1\cos\theta_1 + c\sin\theta_1\cos\theta_2]\,\hat{\mathbf{i}} \\ & - [r_2\theta_2 + c\sin\theta_2]\,\hat{\mathbf{j}} + [(r_1+r_2)\cos\theta_1 + r_1\theta_1\sin\theta_1 + c\cos\theta_1\cos\theta_2]\,\hat{\mathbf{k}}\end{aligned} \tag{3.21}$$

The derivation of the position vectors described in Eqs. 3.20-3.21 is cumbersone and quickly becomes complicated. That is, however, until the planar assumption is applied. Both equations

include the term $\frac{\delta\theta_1}{\delta\theta_2}$, or the change of $\theta_1$ with respect to $\theta_2$. As these two separate DoFs are independent of each other, those terms equal zero and can be eliminated. The virtual displacements then become Eqs. 3.22-3.23.

$$\delta\mathbf{r_{in}} = \left\{ [b\sin\theta_1\cos\theta_2]\,\hat{\mathbf{i}} - [r_2 + b\sin\theta_2]\,\hat{\mathbf{j}} + [b\cos\theta_1\cos\theta_2]\,\hat{\mathbf{k}} \right\} \delta\theta_2 \tag{3.22}$$

$$\delta\mathbf{r_{out}} = \left\{ [-c\sin\theta_1\sin\theta_2]\,\hat{\mathbf{i}} - [r_2 + c\cos\theta_2]\,\hat{\mathbf{j}} - [c\cos\theta_1\sin\theta_2]\,\hat{\mathbf{k}} \right\} \delta\theta_2 \tag{3.23}$$

The corresponding virtual work terms are shown in Eqs. 3.24-3.25.

$$\delta\mathbf{W_{in}} = -F_{in}\,(b\cos\theta_1\cos\theta_2)\,\delta\theta_2 \tag{3.24}$$

$$\delta\mathbf{W_{out}} = F_{out}\,[\sin\theta_1\sin\theta_2\,(c\sin\theta_1\sin\theta_2) + \cos\theta_2\,(r_2 + c\cos\theta_2) + \cos\theta_1\sin\theta_2\,(c\cos\theta_1\sin\theta_2)]\,\delta\theta_2 \tag{3.25}$$

Using trigonometric identities, Eq. 3.25 simplifies conveniently to

$$\delta\mathbf{W_{out}} = F_{out}\,[r_2\cos\theta_2 + c]\,\delta\theta_2 \tag{3.26}$$

Finally, summing the two separate virtual work terms and rearranging, the mechanical advantage in the $y-z$ plane is

$$\frac{F_{out}}{F_{in}} = \frac{b\cos\theta_1\cos\theta_2}{r_2\cos\theta_2 + c} \tag{3.27}$$

The mechanical advantage for the purely planar case where $\theta_1 = 0$ can be seen in Fig. 3.6(b). As the planar and 3D derivations ultimately yield the same equations it is no surprise that they plot the same curve. Unlike the $x-z$ plane, the mechanical advantage never goes negative. It does however approach zero at the extremes of its angular displacement.

Figure 3.7 shows how the 3D derivations of can be used to find the mechanical advantage for these two cases as functions of both $\theta_1$ and $\theta_2$. Equation 3.27 is applied where $\theta_1$ is no longer

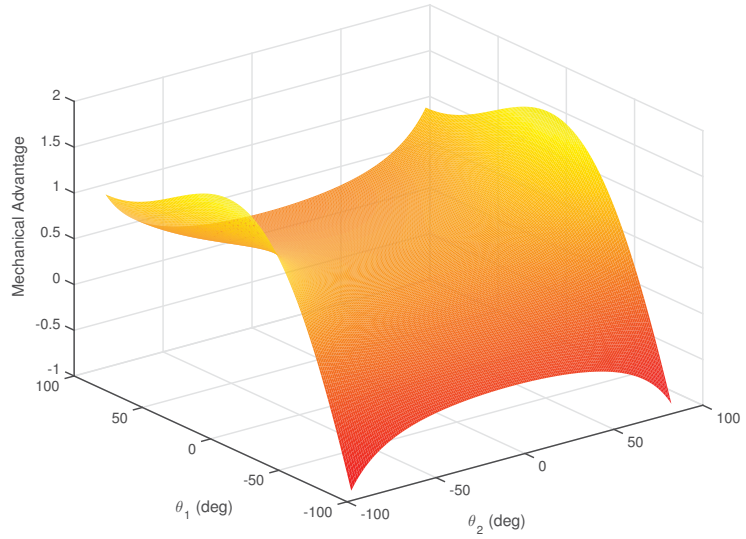


(a) Follower force in the $x-z$ plane

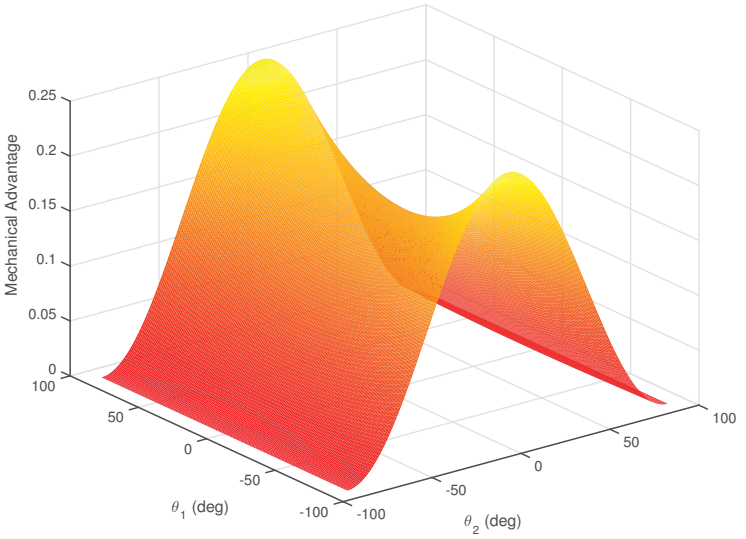


(b) Follower force in the $y-z$ plane

Figure 3.7: Mechanical advantage for follower forces acting in either the $x-z$ or the $y-z$ planes as both $\theta_1$ and $\theta_2$ vary from $\pm 90^\circ$.

held constant. The result is the surface shown in Fig. 3.7(b). An analogous approach is used with Eq. 3.17 to produce the surface shown in Fig. 3.7(a).

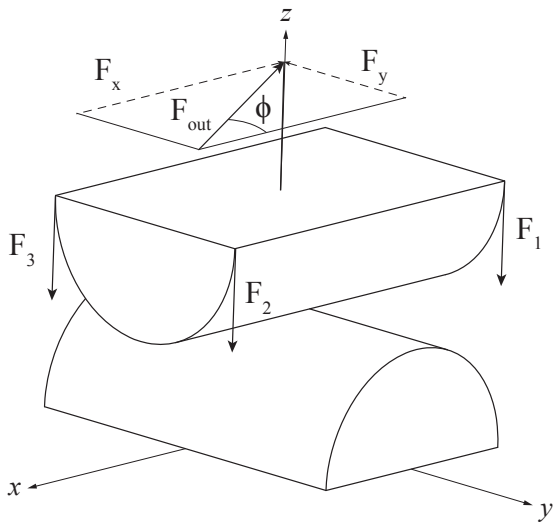


Figure 3.8: Location of input and output forces in 3 dimensions where $F_x$ and $F_y$ are components of $F_{out}$. The input forces $F_1$-$F_3$ are applied at the corners of the platform

### 3.5.2 Force Relations in 3 Dimensions

While the input-to-output relationships in two dimensions are useful, the relationships in three dimensions are also needed. The illustration in Fig. 3.8 shows the parameters of interest. The output $F_{out}$ is a follower force applied at some elevation $c$ above the platform surface. In the neutral position ($\theta_1$ and $\theta_2 = 0$) it has components in both the $x$ and $y$ directions. As it is defined as a follower force, $F_{out}$ will always remain in a plane parallel to the platform surface. There would likely be four actuation cables attached to the corners of the platform, however, only three would be providing resistance against the output at any one time as shown in Fig. 3.8. The angle $\phi$ defines the location between the $x-z$ and $y-z$ planes where the output force acts. For the special cases $\phi = 0$ or $90^\circ$ the problem simplifies to one of the two planar cases presented previously.

The input forces derived for both the planar cases are combinations of two forces at the corners of the platform. Four actuation cables would likely be placed at the corners as shown in Fig. 3.8.

When the crossed cylinders wrist experiences an applied output force with components in both the $x-z$ and $y-z$ planes, there would be opposing forces in three of the four cables. The three forces ($F_1$, $F_2$, and $F_3$) correspond with the engaged cables are shown in Fig. 3.8. The solutions for the planar cases can be combined to solve for the input (actuation) forces required for a desired

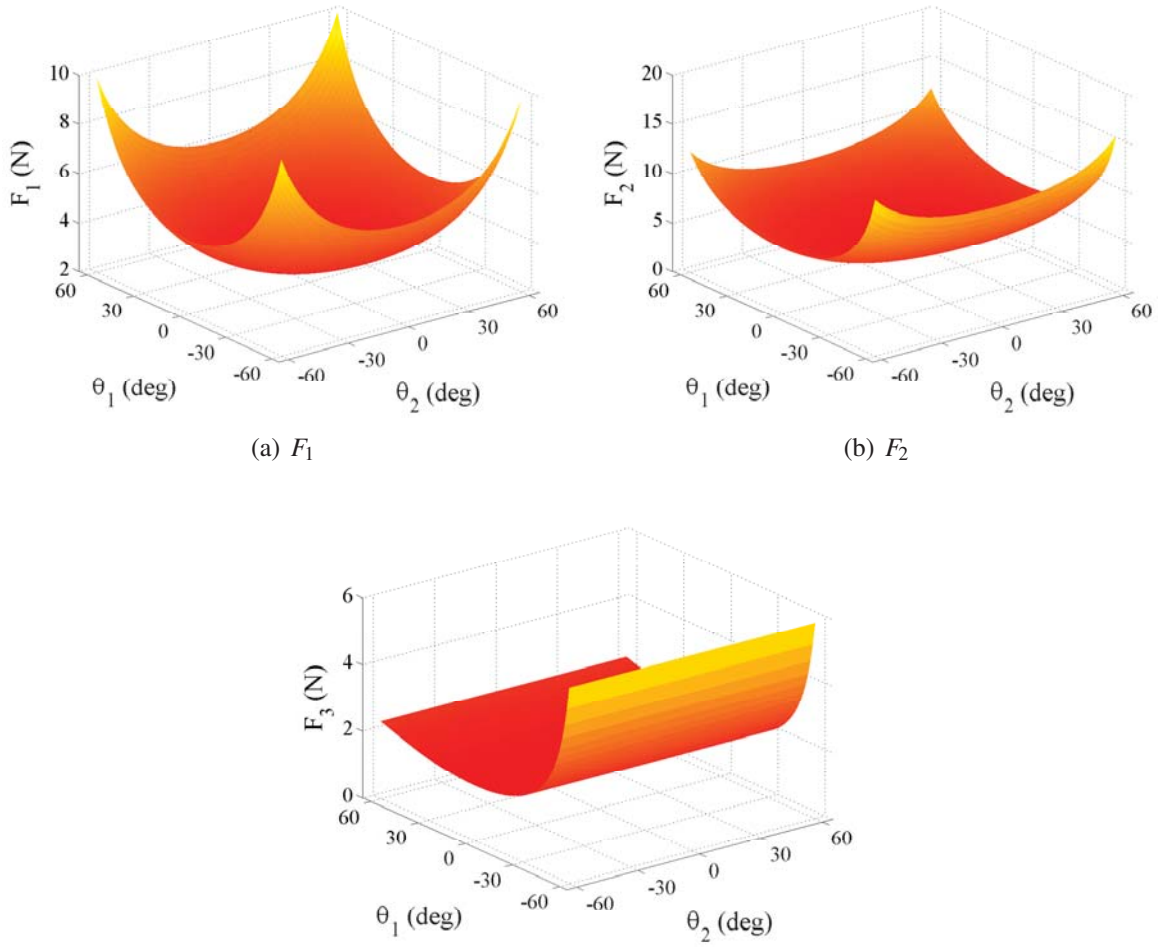


(a) $F_1$ (b) $F_2$

(c) $F_3$

Figure 3.9: Three input forces as functions of $\theta_1$ and $\theta_2$ ($F_o = 2$ N, $\phi = 30°$)

output force. For the purpose of illustration, an output force of 2 N has been chosen to represent a likely loading condition for a 3 mm instrument. The angle $\phi$ (Fig. 3.8) has been set arbitrarily to 30°.

The values for $F_{in}$ solved for previously are broken down into components and then recombined to arrive at expressions for $F_1$, $F_2$, and $F_3$. $F_3$ equals half of $F_{in}$ for the $x-z$ plane. Similarly, $F_1$ equals half of $F_{in}$ for the $y-z$ plane. This is due to the symmetry about the center of the joint. $F_2$ is the sum of $F_1$ and $F_3$ as it contributes to both sets of planar motion. The three charts shown in Fig. 3.9 represent the force that must be applied at each corner to achieve the desired (in this case 2 N) output.

The angle $\phi$ can be varied from 0 to 90° and it will have a predictable impact on the three input forces. As $\phi$ approaches 0, $F_2$ and $F_3$ increase in magnitude as they provide more of the resistance against the output force. Conversely, $F_1$ and $F_2$ will increase in magnitude as $\phi$ approaches 90°.

Because of symmetry, the results shown here can be applied to any corner of the crossed cylinders wrist. When applied to the diagonal corner the results will are identical. For the other two corners the positions for $F_1$ and $F_3$ will be switched but the magnitudes will be the same.

### 3.6 Gear Tooth Stresses

It is important to characterize the load carrying capabilities of the gearing to define the limits of the mechanism. As the loading conditions deviate far from typical gearing configurations, the problem has been simplified significantly. The approach is to find the maximum load allowable for a single gear tooth in several loading scenarios. This provides a conservative baseline for the magnitude of loads that the mechanism is capable of carrying.

For this analysis a particular geometry and material was selected to simulate the crossed cylinders in use as a surgical instrument. A radius of 1.5 *mm* was chosen as it represents a size suitable for a 3 *mm* instrument diameter and 17-4 H900 stainless steel is a popular material in many surgical devices due to its high strength and hardness. A yield strength of $1,379$ *MPa*, elastic modulus of 197 *GPa*, and poisson's ratio of 0.3 were used as parameters to yield a quantitative analyis.

Figure 3.10 shows the maximum loads that can be applied to a single tooth as a function of the number of teeth on the mechanism. The red marker in each chart indicates the max stress for the mechanism as configured with four gear teeth on each row. The compressive load is calculated using the stress over the area, while the bending stress is derived from the Lewis Bending Equation [28].

There is an inverse relationship between the number of teeth and the maximum allowable applied load. This is due to the changing cross-sectional area of the individual tooth. Additionally, the load can be adjusted by the contact ratio between the base and the platform. This ratio is the number of teeth that are engaged at a point in time, effectively increasing the load capacity of the mechanism [28]. Using the contact ratio as a scaling factor, Fig. 3.10(a) shows that a tooth is

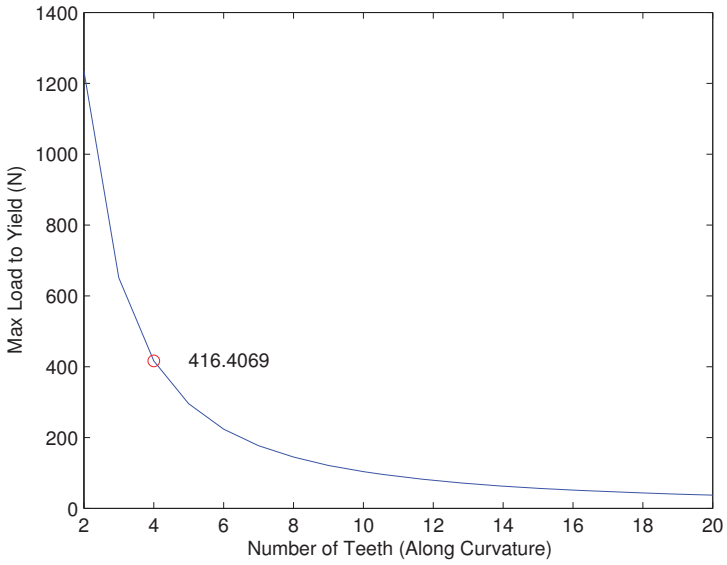


(a) Compression

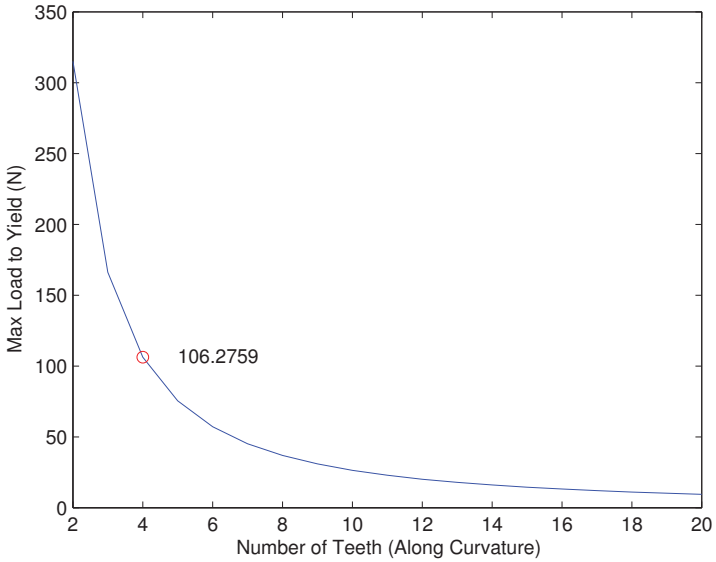


(b) Bending

Figure 3.10: Maximum allowable stresses for a single gear tooth

capable of a compressive load of 416 N (93.5 lb) and similarly, Fig. 3.10(b) shows a maximum bending capacity of 106 N (23.8 lb) for a four-tooth mechanism.

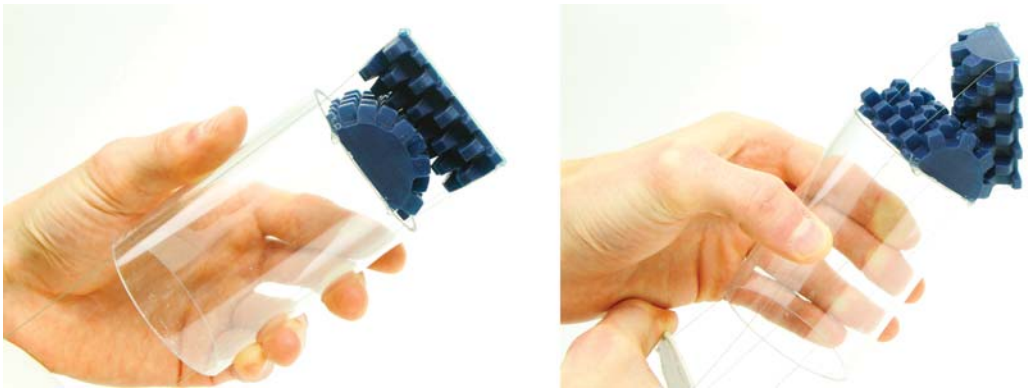

Figure 3.11: Crossed Cylinders wrist mounted to a cylinder to illustrate a potential method of implementation

## 3.7 Implementation

The prototype shown in Fig. 3.11 illustrates how the crossed cylinders wrist could be implemented practically. The base of the joint would be grounded to the shaft of the instrument and four cables would be attached at each corner of the platform to keep the joint in compressive contact during actuation. The cables would be routed between the sides of the joint and the instrument shaft.

## 3.8 Conclusion

The crossed cylinders wrist is a highly compact 2 DoF wrist with a platform well suited for placing an additional gripping mechanism. The compact nature of the mechanism could allow the instrument to operate in volumes much more restricted than the comparatively open scenarios encountered in abdominal procedures.

# CHAPTER 4. MANUFACTURING OF MESO-SCALE SURGICAL INSTRUMENTS

Traditional manufacturing processes are one of the limiting factors in the size of existing surgical instruments. The parts often have features on the order of fractions of a millimeter which means that only the most high-precision processes are suited for production. The combination of alternative mechanisms that reduce part count and friction with high precision manufacturing methods allows for mesoscale instruments to become a reality. This chapter surveys candidate manufacturing methods and the challenges and benefits associated with each. Several of the methods are tailored specifically to small scale parts and highly detailed features. Those methods in combination with the simplified mechanism architectures outlined in previous chapters allow actual prototypes to be made at reasonable costs.

## 4.1 Machining

Precision in machining has improved over the years. Previously, creating a complex 3D shape on the order of just a few millimeters in its greatest dimension would have been very unlikely. However, multi-axis CNC machines better suited especially for producing small-scale parts have been developed. Machining is typically cost effective for producing low volume part runs. It becomes increasingly uneconomical when high volumes of parts need to be produced.

Despite the improvements however, the small features required by many of these complex and detailed parts remain a challenge to create. Overhanging features in particular are difficult to produce with traditional machining tools. When creating such fine features the tools must be so small that it also becomes difficult to compensate for their compliance and vibration during the removal of material.

## 4.2 Metal Injection Molding

Metal Injection Molding (MIM) uses metals powders that are melted into a liquid phase and then injected into a mold to create 3D geometries. There are restrictions on the types of features that can be made. Overhangs in particular are difficult to produce without introducing complex molds and cost increasing side pulls.

Similar to plastic injection molding, this process has the greatest advantages when creating a large number of parts. Preliminary analysis shows that the Split CORE, the more simple of the two architectures, could potentially be manufactured using this method. However, there are design considerations that would result in changes to the designs, such as draft angles on many surfaces and a clear parting line. Ideally, these changes would be minimal and would not alter the major function of the design.

Additionally, this process is best when there is uniform wall thicknesses across the entire part to facilitate even cooling across the parts. This may result in challenges for producing both the Split CORE and crossed cylinders as they have complex 3D shapes particularly represented in the bi-directional gearing. These challenges are as yet unexplored and must be addressed to evaluate MIM as a potential production candidate.

## 4.3 Composite Carbon Nanotube Structures

Previous work has also investigated the potential for creating the crossed cylinders at scale using Carbon Nanotube (CNT) structures as shown in Fig. 4.1 [29]. CNT layers are grown to a specified height and assembled layer by layer until the desired 3D shape is created. The CNT structure alone is fairly brittle but there is potential that infiltrating the CNT forests with nickel or other metals could provide the strength required for acceptable performance. Additionally, although the layer by layer assembly is time consuming, it is possible that it could be used once to define the geometry for a mold that could then be used repeatedly for high volume production.

## 4.4 Micro Metal Laser Sintering

Metal Laser Sintering (MLS) is an additive manufacturing process where metal powders are laid down one layer at a time and then sintered together with a high powered laser. Typical

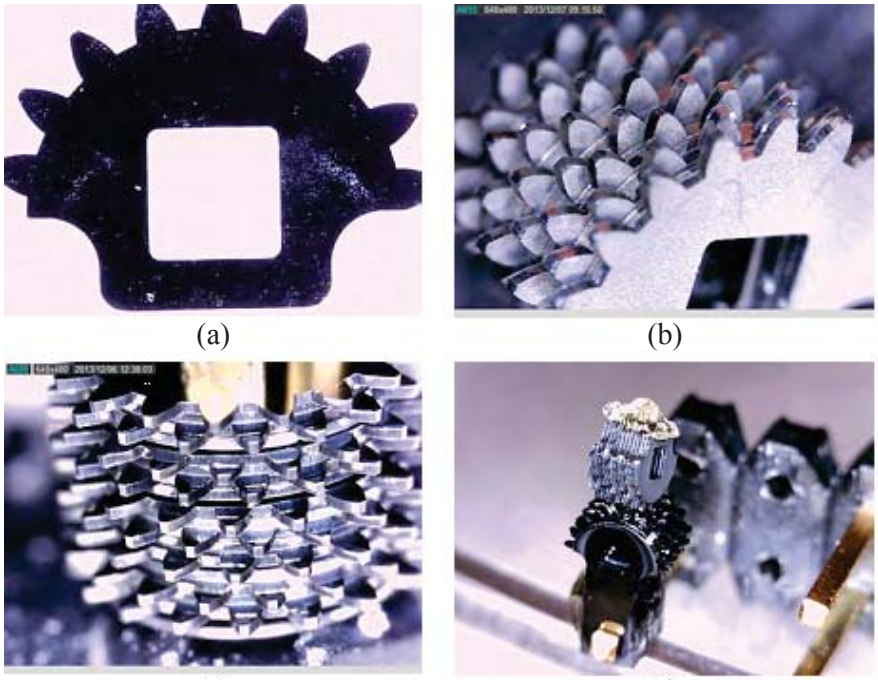


Figure 4.1: CNT crossed cylinders (note that the alignment hole is 1 mm square) a) a single CNT layer b) one half of the joint assembled c) assembly method using an electrical pin d) base and platform interfacing with each other

laser sintering machines however do not have the resolution required to make mesoscale parts accurately.

A micro MLS method has been developed that is specifically tailored to creating highly detailed, small scale parts. Fine metal powders with an average particle size distribution of $< 5\ \mu m$ D90 (at least 90% of the particles are less than 5 $\mu m$ in diameter) are used. This allows the build to achieve tolerances on the order of $\pm 5\ \mu m$ and features as small as 25 $\mu m$. These capabilities represent a great improvement over traditional machining or MIM methods that typically have difficulty accurately defining features much smaller than 100 $\mu m$.

One of the advantages of this process is its fast turn around. While some processes like MIM require expensive tooling to be made before any parts are produced, or others like the CNT composite structures also require lithographically defined masks and careful assembly of each layer, micro MLS merely requires the transfer of a 3D part file and the selection of a material to

begin the production. This is especially cost effective for low volume part runs and the prototyping phases of the design process.

The crossed cylinder has features of such a scale that it lends itself well to micro Metal Laser Sintering (MLS). This process has already proved to be highly advantageous for producing mesoscale parts with features on the order of a few thousandths of an inch. Because of the complex 3D geometry associated with the bi-directional gearing, the parts would be difficult to machine for a number of reasons. Micro MLS would be ideal for such small and complex parts.

## 4.5 Conclusion

By combining high precision production methods with designs that simplify mechanism architectures and reduce sliding friction, the mesoscale instruments presented in previous chapters can be made to function properly. This critical combination allows these instruments to be assembled at such small scales while still retaining their dexterity. Additionally, the use of additive processes like micro MLS can result in very short lead times even in the prototyping phases because there is no need to set up expensive tooling, while the more involved processes like MIM would be more cost effective for long term, high volume runs of more parts. The combination of these methods could result in making these instruments feasible, not only from an engineering standpoint but from clinical and economic standpoints as well.

# CHAPTER 5. CONCLUSIONS

By using non-traditional mechanisms that eliminate pin joints and pulleys the effects of friction are drastically reduced. Both the Split CORE joint and crossed cylinders wrist implement rolling contact and gearing in place of the bearing surfaces used in pin joints. The rolling contact results in more material to carry the loads and the gearing prevents slip while adding very minimal friction to the system.

Manufacturing methods created specifically to produce small parts with detailed features were used to overcome the limitations in traditional processes. Several additive manufacturing methods were employed to allow a greater freedom in part configurations. Overhangs and other features that are otherwise very difficult to achieve were made possible by the use of micro MLS and composite CNT constructions.

Using these methods, full 3 DoF prototype instruments were made at 3, 4, and 5 mm diameter scales—sizes that previously would have been very difficult to achieve. Additionally, not only were the parts manufacturable, but they were made within tolerances such that the parts could actually be assembled.

By reducing the number of parts in an assembly and the number of traditional friction inducing pin joints, mesoscale mechanisms can be drastically simplified. These changes in overall architecture in combination with improved manufacturing methods especially suited for small-scale part production make the practical development of these surgical instruments a reality. Another significant side effect of reducing the number of parts in the assembly is the potential to drastically reduce the overall cost of the wrist and grips for a given instrument. The cost could be reduced drastically enough that single use instruments (desirable because of their lack of need for reprocessing and sterilization) could become practical.

Several fully functional prototypes were created to show their feasibility for actual use in clinical settings. Initial testing showed that they had the dexterity, range of motion, and strength

to contribute significantly to clinical procedures. The instruments were able to handle needles and sutures in a very precise manner while still providing enough force for suturing and other surgical tasks.

These prototypes have the advantage of not only being smaller in diameter, but having significantly shorter wrists than other existing robotic instruments. This means that they travel through their range of motion in a much tighter volume. This feature could open up a wide range of clinical procedures that previously have been too difficult to perform due to the space restrictions. Ear nose and throat, pediatric, or base of the skull procedures all require instruments that can dexterously maneuver in a confined space.

The combination of these benefits have the potential to make highly precise, mesoscale, robot-actuated minimally invasive surgical instruments economically viable products. By making these instruments practical to manufacture and assemble, an increased number of procedures may become minimally invasive and as a result more people can have their ailments treated with drastically reduced impacts to their recovery time and overall health.

## REFERENCES


[1] Ferguson, M. W. J., and O'Kane, S. a., 2004. "Scar–free healing: from embryonic mechanisms to adult therapeutic intervention." *Philosophical Transactions of the Royal Society of London B: Biological Sciences,* **359**(1445), 05, pp. 839–850. 1

[2] Tacchino, R., Greco, F., and Matera, D., 2009. "Single-incision laparoscopic cholecystectomy: surgery without a visible scar." pp. 896–899. 1

[3] Cigaina, V., 2000. Laparoscopic forceps. 1

[4] Fan, P., 2012. Laparoscopic dual grasper. 1

[5] Morley, T., and Wallace, D., 2004. Roll-pitch-roll-yaw surgical tool, Jan. 13 US Patent 6,676,684. 1, 10

[6] Cooper, T., Chang, S., Anderson, S., Williams, D., Manzo, S., and Wallace, D., 2003. Surgical tool having positively positionable tendon-actuated multi-disk wrist joint, Dec. 4. 1

[7] Buysse, S. P., 2008. Laparoscopic bipolar electrosurgical instrument. 1

[8] Liu, X., Tong, J., and Sun, Y., 2007. "Millimeter-sized nanomanipulator with sub-nanometer positioning resolution and large force output." In *Nanotechnology, 2007. IEEE-NANO 2007. 7th IEEE Conference on*, pp. 454–457. 1

[9] Kim, K., Liu, X., Zhang, Y., and Sun, Y., 2008. "Micronewton force-controlled manipulation of biomaterials using a monolithic MEMS microgripper with two-axis force feedback." In *Robotics and Automation, 2008. ICRA 2008. IEEE International Conference on*, pp. 3100–3105. 1

[10] Kim, D.-H., Lee, M. G., Kim, B., and Sun, Y., 2005. "A superelastic alloy microgripper with embedded electromagnetic actuators and piezoelectric force sensors: a numerical and experimental study." *Smart Materials and Structures,* **14**. 1

[11] Beyeler, F., Neild, A., Oberti, S., Bell, D., Sun, Y., Dual, J., and Nelson, B., 2007. "Monolithically fabricated microgripper with integrated force sensor for manipulating microobjects and biological cells aligned in an ultrasonic field." *Microelectromechanical Systems, Journal of,* **16**(1), pp. 7–15. 1

[12] Zubir, M. N. M., Shirinzadeh, B., and Tian, Y., 2009. "A new design of piezoelectric driven compliant-based microgripper for micromanipulation." *Mechanism and Machine Theory,* **44**(12), pp. 2248–2264. 1

[13] Duc, T. C., Creemer, J. F., and Sarra, P. M., 2006. "Lateral nano-newton force-sensing piezoresistive cantilever for microparticle handling." *Journal of Micromechanics and Microengineering,* **16**. 1

[14] Marcincin, J. N., and Smrcek, J., 1997. "Biomechanical grippers: important elements of biomechanical robots." *Industrial Robot: An International Journal,* **24**, pp. 234–238. 1

[15] Zhao, B., and Nelson, C. A., 2013. "Decoupled cable-driven grasper design based on planetary gear theory." *Journal of Medical Devices,* **7**(2), June, pp. 020918–020918. 1

[16] Mei, F., Yili, F., Bo, P., and Xudong, Z., 2012. "An improved surgical instrument without coupled motions that can be used in robotic-assisted minimally invasive surgery." *Proceedings of the Institution of Mechanical Engineers, Part H: Journal of Engineering in Medicine,* **226**(8), pp. 623–630. 1

[17] Manzo, S., and Heaton, L., 2005. Wristed robotic surgical tool for pluggable end-effectors. 1

[18] Cooper, T. G., and Anderson, S. C., 2012. Flexible wrist for surgical tool. 1

[19] Yan Nai, T., Herder, J. L., and Tuijthof, G. J. M., 2011. "Steerable mechanical joint for high load transmission in minimally invasive instruments." *Journal of Medical Devices,* **5**(3), p. 034503. 1

[20] Howell, L., Magleby, S., and Olsen, B., 2013. *Handbook of Compliant Mechanisms*. John Wiley & Sons, Inc., New York, NY. 1

[21] Rogers, T. W., and Williams, M. R., 2008. Roll joint and method for a surgical apparatus. 1

[22] Jung, G.-P., Koh, J.-S., and Cho, K.-J., 2011. "Meso-scale compliant gripper inspired by caterpillar's proleg." In *Robotics and Automation (ICRA), 2011 IEEE International Conference on*, pp. 1831–1836. 1

[23] Eisinberg, A., Tonet, O., Dario, P., Macri, G., and Carrozza, M., 2006. "Microfabricated instruments for fetal cardiac surgery: Experiments on haptic tissue recognition." In *Haptic Interfaces for Virtual Environment and Teleoperator Systems, 2006 14th Symposium on*, pp. 273–279. 1

[24] Krecinic, F., Duc, T. C., Lau, G. K., and Sarro, P. M., 2008. "Finite element modelling and experimental characterization of an electro-thermally actuated silicon-polymer micro gripper." *Journal of Micromechanics and Microengineering,* **18**(6). 1

[25] Halverson, P. A., Howell, L. L., and Magleby, S. P., 2010. "Tension-based multi-stable compliant rolling-contact elements." *Mechanism and Machine Theory,* **45**(2), pp. 147–156. 5

[26] Jelinek, F., Pessers, R., and Breedveld, P., 2013. "Dragonflex-smart steerable laparoscopic instrument." *Journal of Medical Devices,* **7**, June, pp. 1–2. 5

[27] Howell, L. L., 2001. *Compliant Mechanisms*. John Wiley & Sons, Inc., New York, NY. 7

[28] Budynas, R. G., and Nisbett, J. K., 2011. *Shigley's Mechanical Engineering Design, Ninth Edition*. McGraw-Hill. 13, 42

[29] Tanner, J. D., Grames, C., Jensen, B. D., Magleby, S. P., and Howell, L. L., 2015. "Millimeter-scale robotic mechanisms using carbon nanotube composite structures." *Journal of Mechanisms and Robotics,* **7**(2), 05, pp. 021001–021001. 28, 46

# APPENDIX A. DERIVATION OF MECHANICAL ADVANTAGE (SPLIT CORE)

## A.1 Derivation of Mechanical Advantage

Two input forces exist in this design, $F_1$ (as shown in Fig. 2.2) and $F_2$. If the actuating cables attached at the points of $F_1$ and $F_2$ are connected to a common spool, then it is assumed that as a force is applied to one cable the force in the opposite cable goes to zero. Under this assumption, if $F_1$ equals 2 N then $F_2$ is zero and therefore not illustrated. In addition to this assumption Fig. 2.2 shows that for any nonzero value of $F_{out}$, $F_1$ will also be nonzero, and consequently $F_2$ will be zero. This is because $F_1$ is the only force that can balance the system. If considering the other jaw in the assembly (not shown in Fig. 2.2), for any nonzero value of $F_{out}$, $F_2$ would be nonzero and $F_1$ would be zero. The derivations that follow apply to the case shown in Fig. 2.2 where $F_2$ is zero. However, the same approach can be used to consider the case for the opposite jaw.

The method of virtual work can be used to determine the magnitude of $F_1$ for given values of $F_{out}$ and $\theta_j$. The first step in calculating the virtual work in the system is choosing a generalized coordinate. The jaw angle, $\theta_j$, is a convenient parameter because it is used to describe the position of the jaw, and because the expression for $F_1$ will be derived as a function of $\theta_j$. Therefore, $\theta_j$ will be used as the generalized coordinate. Next, each of the applied forces are written in vector form in terms of the generalized coordinate. The directions of the forces are shown in Eqs. A.1 and A.2 for $F_{out}$ and $F_1$, respectively.

The input force in this model is placed at some distance $d_f$ from the corner of the upper segment and is directed toward a point a distance $d_f$ from the corresponding corner of the lower segment. This assumption is based on the idea that cables provide the input forces and route around the lower geometry before entering the shaft and connecting to the control interface at the opposite end of the instrument. The reason for placing the input force some distance from the corner is to increase the moment arm, and consequently the mechanical advantage. This is particularly important when the point of rolling contact is near the corners of the segments (i.e. as

$\theta_c$ approaches $\theta_r$). However, in this configuration it is also important to address any interference that may result from placing the forces and cables at these locations. Using this assumption

$$\mathbf{F_{out}} = F_{out}\left(-\cos\theta_j\hat{\mathbf{i}} - \sin\theta_j\hat{\mathbf{j}}\right) \tag{A.1}$$

$$\mathbf{F_1} = F_1\left(\sin\frac{\theta_j}{2}\hat{\mathbf{i}} - \cos\frac{\theta_j}{2}\hat{\mathbf{j}}\right) \tag{A.2}$$

Next, position vectors are written from the origin, $O$, to each of the applied forces. The vector describing the location of $Z_{out}$ is straightforward to describe in terms of $\theta_j$ as

$$\mathbf{Z_{out}} = \left[-2r_1\sin\frac{\theta_j}{2} - \left(L_j - r_1\cos\theta_r\right)\sin\theta_j\right]\hat{\mathbf{i}} + \left[2r_1\cos\frac{\theta_j}{2} + \left(L_j - r_1\cos\theta_r\right)\cos\theta_j\right]\hat{\mathbf{j}} \tag{A.3}$$

The other vector is more complicated because it lies at a point on the arc determined by $\theta_r$, and that point is a fraction of $\theta_j$. The position vector locating $\mathbf{Z_1}$ can be found by summing the vector from point $O$ to point $A$ and the vector from point $A$ to the location of force application. This results in the vector describing the position of $Z_1$ as

$$\mathbf{Z_1} = -2r_1\sin\frac{\theta_j}{2}\hat{\mathbf{i}} + 2r_1\cos\frac{\theta_j}{2}\hat{\mathbf{j}} + \begin{bmatrix}\cos\theta_j & -\sin\theta_j\\ \sin\theta_j & \cos\theta_j\end{bmatrix}\begin{bmatrix}r_1\sin\theta_r\hat{\mathbf{i}}\\ -r_1\cos\theta_r\hat{\mathbf{j}}\end{bmatrix} \tag{A.4}$$

Equation A.4 can be expanded to its $\hat{\mathbf{i}}$ and $\hat{\mathbf{j}}$ components and then simplified. Doing this results in Eq. A.5.

$$\mathbf{Z_1} = \left[-2r_1\sin\frac{\theta_j}{2} + r_1\sin\left(\theta_j + \theta_r\right)\right]\hat{\mathbf{i}} + \left[2r_1\cos\frac{\theta_j}{2} - r_1\cos\left(\theta_j + \theta_r\right)\right]\hat{\mathbf{j}} \tag{A.5}$$

The virtual displacements associated with eqs. 2.4-2.5 is their partial derivatives with respect to the generalized coordinate.

$$\delta\mathbf{Z} = \frac{dZ}{d\theta_h}\delta\theta_j \tag{A.6}$$

$$\delta \mathbf{Z_{out}} = \left\{ \left[ -r_1 \cos\frac{\theta_j}{2} - \left(L_j - r_1 \cos\theta_r\right)\cos\theta_j \right] \hat{\mathbf{i}} + \left[ -r_1 \sin\frac{\theta_j}{2} - \left(L_j - r_1 \cos\theta_r\right)\sin\theta_j \right] \hat{\mathbf{j}} \right\} \delta\theta_j \tag{A.7}$$

$$\delta \mathbf{Z_1} = \left\{ \left[ -r_1 \cos\frac{\theta_j}{2} + r_1 \cos\left(\theta_j + \theta_r\right) \right] \hat{\mathbf{i}} + \left[ -r_1 \sin\frac{\theta_j}{2} + r_1 \sin\left(\theta_j + \theta_r\right) \right] \hat{\mathbf{j}} \right\} \delta\theta_j \tag{A.8}$$

The virtual work associated with each force is determined by calculating the dot product of each force vector (Eqs. 2.2 and A.2) and its respective virtual displacement vector.

$$\delta W = \mathbf{F} \cdot \delta \mathbf{Z} \tag{A.9}$$

$$\delta W_{out} = F_{out} \left( r_1 \cos\frac{\theta_j}{2} - r_1 \cos\theta_r + L_j \right) \delta\theta_j \tag{A.10}$$

$$\delta W_1 = -F_1 r_1 \sin\left(\theta_r + \frac{\theta_j}{2}\right) \delta\theta_j \tag{A.11}$$

The sum of these dot products is the total virtual work in the system. For a system in equilibrium, the total virtual work is equal to zero.

$$0 = \left[ F_{out} \left( r_1 \cos\frac{\theta_j}{2} - r_1 \cos\theta_r + L_j \right) - F_1 r_1 \sin\left(\theta_r + \frac{\theta_j}{2}\right) \right] \tag{A.12}$$

This makes it possible to rearrange the equation to determine $F_1$ for various values of $F_{out}$ and $\theta_j$.

$$F_1 = \frac{F_{out}\left(\cos\frac{\theta_j}{2} - \cos\theta_r + \frac{L_j}{r_1}\right)}{\sin\left(\theta_r + \frac{\theta_j}{2}\right)} \tag{A.13}$$

*

Including a Preload Force In most cases a preload force is applied along with the actuation forces (Fig. 2.2). If an equal preload force is applied to both sides of the mechanism (i.e. equal preload in both actuation cables) then the changes to the previous derivations are relatively simple. The input force term, $F_1$, is replaced by $(F_1 + F_p)$ where $F_p$ is the preload force. The virtual work derivation would also include the effects of $F_p$ at the location of $F_2$. Doing this results in a slightly different result.

$$F_1 = \frac{F_{out}\left(\cos\frac{\theta_j}{2} - \cos\theta_r + \frac{L_j}{r_1}\right) - 2F_p r_1 \cos\theta_r \sin\frac{\theta_j}{2}}{\sin\left(\theta_r + \frac{\theta_j}{2}\right)} \tag{A.14}$$

The inclusion of a preload force exhibits two interesting behaviors. First, the required input force is reduced when $\theta_j$ is between 0 and 90°, but is increased when $\theta_j$ is between 0 and $-90°$. Second, for $\theta_r = 90°$ the preload force has no effect on the required input force and Eq. A.14 becomes equivalent to Eq. A.13.

*

Example Design To demonstrate the use of these equations of motion, consider a design where the desired jaw rotation is $\pm 90°$ with a jaw length of 6.25 mm and a desired output force of 2 N. Assume that there is not a preload force in the cables. To achieve this motion $\theta_r$ must be at least 45°. To provide reasonable structural support at the extremes of motion, we will choose $\theta_r = 60°$.

In this example, we will design the instrument to fit within a 3 mm circle so that it can be attached to a 3 mm shaft. To do this, we can assume that the base of Split CORE joint is square. Therefore, one side of the square is equal to $2r_1 \sin\theta_r$. The diagonal of the square will be equal to the diameter of the desired shaft size (3 mm). Using this information $r_1$ is calculated as follows:

$$(3mm)^2 = 2\left(2r_1 \sin\theta_r\right)^2 \tag{A.15}$$

$$r_1 = \sqrt{\frac{9}{8\sin^2\theta_r}} = 1.23\ mm \tag{A.16}$$

The distance from the upper segment to the point of force application ($d_f$) must also be determined (see Fig. 2.2). This distance is defined here as the point where the force would be applied if $\theta_r$ were equal to 90°. This gives the design the same mechanical advantage as a traditional CORE mechanism, but its overall height is reduced because the actual profile is defined by $\theta_r = 60°$. Therefore, $d_f$ is

$$d_f = r_1(1 - sin_r) = 0.165mm \tag{A.17}$$

The resulting input force, $F_1$, can be determined for any jaw rotation using Eq. 2.6. The value of $\theta_r = 90°$ will be used because that defines the location of force input. For other calculations, such as segment height and range of motion, $\theta_r = 60°$ would be used. Figure 2.4 shows the required input force for a range of $\theta_j$ from $-90°$ to 90°. This plot shows that the required force is symmetric about $\theta_j = 0$ and ranges between approximately 12 and 16 N. The locations of greatest force are at the extremes of motion. This is to be expected because it is where the moment arm of force application is minimized. A plot of the mechanical advantage, shown in Fig. 2.5, also illustrates this concept where mechanical advantage is maximum at $\theta_j = 0$.

In addition to the force requirements, mechanical advantage also gives some insight into the control and precision of the instrument. Mechanical advantage can be used to describe the relationship between input displacement and output displacement. In this particular design, the input displacement is the amount of motion in the actuation cable. The output displacement corresponds to the displacement of the tip of the jaw where $F_{out}$ is positioned (see Fig. 2.2). For the example design given, this means that when $\theta_j = 0$ (where M.A. = 0.164) a 1 mm displacement of the actuation cable would result in an output displacement of approximately 6.10 mm. This is based on the following relationship:

$$MA = \frac{input\ displacement}{output\ displacement} \tag{A.18}$$

There are several ways to maximize precision and control of the instrument tip. One way is to increase the mechanical advantage of the system. This can be done by increasing the radius of curvature in the upper and lower segments ($r_1$). Another way to accomplish improved control is to reduce the diameter of the spool which is used to actuate the cable. With a smaller diameter spool, a given rotational input will result in a smaller cable displacement than would occur with the same rotational input on a larger spool. This method does not change the required input force (or mechanical advantage) but it does improve the control of the motion at the jaw tip.